Crystal Temperature Control in the Czochralski Crystal Growth Process

Antonios Armaou and Panagiotis D. Christofides
Dept. of Chemical Engineering, University of California, Los Angeles, CA 90095

This work proposes a control configuration and a nonlinear multivariable model-based feedback controller for the reduction of thermal gradients inside the crystal in the Czochralski crystal growth process after the crystal radius has reached its final value. Initially, a mathematical model which describes the evolution of the temperature inside the crystal in the radial and axial directions and accounts for radiative heat exchange between the crystal and its surroundings and motion of the crystal boundary is derived from first principles. This model is numerically solved using Galerkin's method and the behavior of the crystal temperature is studied to obtain valuable insights which lead to the precise formulation of the control problem, the design of a new control configuration for the reduction of thermal gradients inside the crystal and the derivation of a simplified 1-D in a space dynamic model. Then, a model reduction procedure for partial differential equation systems with time-dependent spatial domains (Armaou and Christofides, 1999) based on a combination of Galerkin's method with approximate inertial manifolds is used to construct a fourth-order model that describes the dominant thermal dynamics of the Czochralski process. This low-order model is employed for the synthesis of a fourth-order nonlinear multivariable controller that can be readily implemented in practice. The proposed control scheme is successfully implemented on a Czochralski process used to produce a 0.7 m long silicon crystal with a radius of 0.05 m and is shown to significantly reduce the axial and radial thermal gradients inside the crystal. The robustness of the proposed controller with respect to model uncertainty is demonstrated through simulations.

Introduction

Czochralski crystal growth (CZ) is a well-established industrial process used for the production of single crystals like silicon (Si) and gallium arsenide (GaAs). Such crystals are widely used for the construction of wafers employed in the production of microelectronic chips. The central idea of the CZ process is to grow a crystal from a melt by pulling a seed crystal very slowly within a well-regulated thermal environment in a furnace. For the subsequent processing steps, it is important to form a cylindrical crystal with desired radius and length of dimensions which includes very low concentrations of impurities and dislocations, as well as a uniform dopant distribution.

The current practice in achieving a constant crystal radius is to use a proportional-integral-derivative (PID) controller that manipulates the pulling rate of the crystal from the melt to adjust the crystal radius, while the regulation of the crystal temperature is addressed by adjusting the heat transferred to the melt and crystal by manipulation (typically via PID) of the heater power. The tuning of such PID controllers based on fundamental lumped parameter models that describe the dominant dynamic characteristics of the CZ process has been addressed in a series of articles (Gevelber, 1994a,b; Gevelber and Stephanopoulos, 1987; Gevelber et al., 1987, 1988). Even though these works provide valuable insights for the nature or the crystal radius and thermal dynamics, and identify natural control objectives and variables, as well as structural limitations on the best achievable closed-loop performance, they do not account for the presence of spatial variations of the

Correspondence concerning this article should be addressed to P. D. Christofides.

temperature inside the crystal which constitute the main cause for dislocations and defects (Szabó, 1985; Gevelber, 1994a). Furthermore, PID controllers do not account for the fact that CZ processes exhibit nonlinear and time-varying behavior and involve coupling of variables evolving in widely different time-scales. In an effort to overcome the limitations of conventional controllers, the problems of controlling the radius of the crystal and reducing the thermal strain in the interface between crystal and melt were recently addressed within a model predictive control framework (Irizarry-Rivera and Seider, 1997a,b). However, in these articles the key practical issued of deriving accurate low-order approximations of the distributed process model that can be used in real-time control implementation was not addressed.

The main challenge in the design of model-based feedback controllers for CZ processes is the fact that the dynamic models of such processes are typically in the form of nonlinear parabolic partial differential equations (PDEs) with time-dependent spatial domains. These are distributed parameter (infinite-dimensional) systems, and therefore, they cannot be directly used for the design of practically implementable (low-dimensional) controllers. The main feature of parabolic PDEs is that the eigenspectrum of the spatial differential operator can be partitioned into a finite-dimensional slow one and an infinite-dimensional stable fast complement. Therefore, the standard approach to synthesize feedback controllers for parabolic PDEs (Balas, 1979; Chen and Chang, 1992) involves initially the application of standard Galerkin's method to the PDE system to derive ODE systems that accurately describe its dominant dynamics. These ODE systems are subsequently used as the basis for the synthesis of finite-dimensional controllers. A potential drawback of this approach is that the number of modes that should be retained to derive an ODE system which yields the desired degree of approximation may be very large, thereby leading to complex controller synthesis and high dimensionality of the resulting controllers.

To overcome these controller synthesis and implementation problems, recent research efforts have focused on the synthesis of low-order controllers for parabolic PDE systems by taking advantage of the concept of inertial manifold (IM) (Temam, 1988). If it exists, an IM is a positively invariant, exponentially attracting, finite-dimensional Lipschitz manifold. When the trajectories of the PDE system are on the IM, then this system is exactly described by a low-order ODE system (called inertial form), which can be used for the synthesis of low-order controllers. However, the use of the inertial form for controller synthesis is limited due to the fact that the computation of the closed-form expression of the IM is impossible for most practical applications. This limitation motivated the development of efficient procedures for the construction of accurate approximations of the function that describes the inertial manifold (called approximate inertial manifolds (AIMs)) (see, for example, Foias et al., 1989; Christofides and Daoutidis, 1997; Shvartsman and Kevrekidis, 1998). These developments led to the synthesis of low-order nonlinear output feedback controllers that enforce closed-loop stability and output tracking in quasi-linear parabolic PDE systems (Christofides and Daoutidis, 1997); the reader may also refer to the recent book (Christofides, 2001) for more references and results in this area.

In the area of feedback control of parabolic PDE systems with time-dependent spatial domains, previous research has focused on the design of linear distributed optimal controllers (Wang, 1967, 1990), as well as the synthesis of nonlinear distributed state estimators using stochastic methods (Ray and Seinfeld, 1975). In a previous work (Armaou and Christofides, 1999), we proposed a general method for the synthesis of nolinear time-varying output feedback controllers that enforce stability and output tracking in the closed-loop infinite-dimensional system. The controllers were synthesized on the basis of low-order approximations of the PDE system obtained through combination of Galerkin's method and approximate inertial manifold concepts which were developed for time-varying infinite-dimensional systems.

This work proposes a control configuration and a nonlinear multivariable model-based feedback controller for the reduction of thermal gradients inside the crystal in the Czochralski crystal growth process after the crystal radius has reached its final value. Even though the process model is a distributed system, the proposed controller is of low-order, and, therefore, it can be readily implemented in real time.

This article is structured as follows. A fundamental mathematical model which describes the evolution of the temperature inside the crystal in the radial and axial directions and accounts for radiative heat exchange between the crystal and its surroundings and motion of the crystal boundary is initially presented. This model is numerically solved using Galerkin's method and the behavior of the crystal temperature is studied to obtain valuable insights which lead to the precise formulation of the control problem and the derivation of a simplified one-dimensional in space PDE model with moving domain which is used for controller synthesis. Then, a general nonlinear model reduction and control method for PDE systems with moving domains developed in (Armaou and Christofides, 1999) is briefly presented. This method is used to construct a fourth-order model that describes the dominant thermal dynamics of the Czochralski process and synthesize a fourth-order nonlinear controller that can be readily implemented in practice. The proposed control scheme is successfully implemented on a Czochralski process used to produce a 0.7 m long silicon crystal with a radius of 0.05 m and is shown to significantly reduce the axial and radial thermal gradients inside the crystal compared to the open-loop operation and to the case of using a single control actuator. The robustness of the proposed controller with respect to parametric model uncertainty, melt and chamber temperature disturbances, and unmodeled actuator and sensor dynamics is demonstrated through simulations.

Czochralski Crystal Growth: Modeling of Crystal Thermal Behavior

We focus on a Czochralski crystal growth process shown in Figure 1 used to produce a 0.7 m long silicon crystal with a radius of 0.05 m. The process is comprised of a cylindrical chamber which includes a rotating pedestal that can move in the axial direction. A crucible containing silicon (Si) crystals is placed on the pedestal and heaters (placed on the sides of the chamber and under the pedestal) are used to increase the temperature of the Si crystals inside the crucible (through

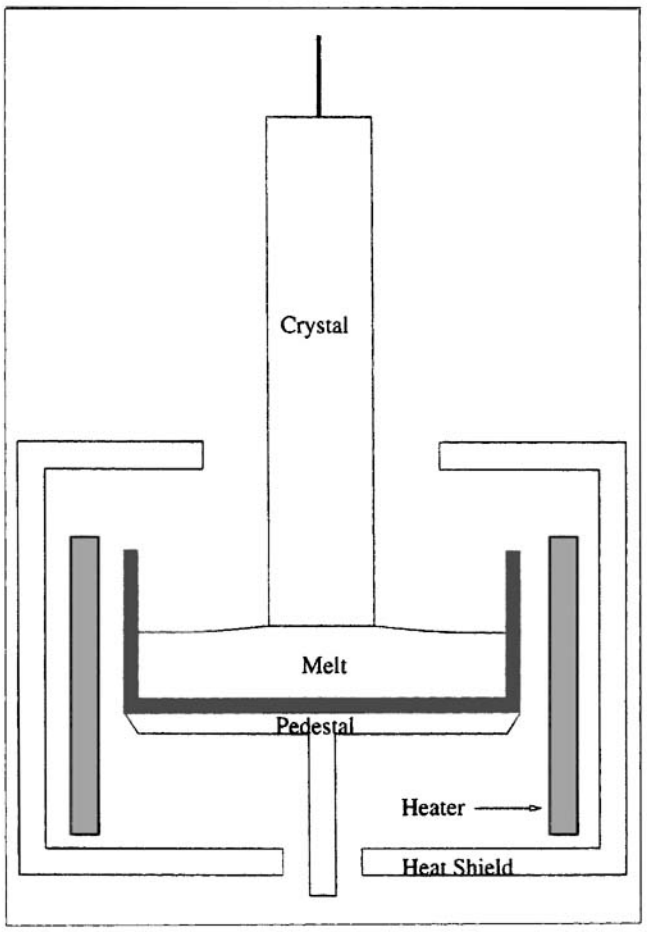

Figure 1. Czochralski crystal growth.

radiation) above the melting point of *Si*. A *Si* seed crystal comes in contact with the melt and the temperature of the melt is adjusted until the meniscus is supported by the end of the seed. Once the meniscus has been stabilized, the seed crystal is pulled away from the melt and new crystal is formed (Hurle, 1994). The interface between the crystal and the melt is maintained at a constant position during the operation of the process by moving the position of the pedestal higher with time. As the length of the crystal becomes larger, part of it leaves the chamber and starts cooling, at which point the thermal gradients inside the crystal become large and may cause thermal strain inside the crystal (Szabó, 1985). If the cooling conditions are not properly regulated, large thermal strain may cause microdefects (such as, dislocations) inside the crystal, and may even lead to fracture. As a result, the cooling process should be carefully regulated. Finally, the process is terminated when the crystal-melt interface reaches the crucible bottom.

The development of detailed mathematical models for the Czochralski crystal growth process is an area that has received significant attention (see, for example, Hurle, 1994), and at this point, comprehensive models are available (Derby and Brown, 1986a,b, 1987; Atherton et al., 1987; Derby et al., 1987; Zhou et al., 1994; Van den Bogaert and Dupret, 1997a,b). Since the objective of our work is to develop a control configuration and a model-based feedback controller which will smoothly regulate the cooling process of the crystal as it leaves the chamber, our modeling effort focuses on the development of a mathematical model that describes the spatiotemporal evolution of the crystal temperature, after the crystal radius has obtained its final value, and accounts for radiative heat exchange between the crystal, heater shield, crucible, melt surface and the environment. Moreover, our control objective allows making the following simplifying assumptions in the model development; (a) the crystal radius and the meniscus height are assumed to be constant; this is typically achieved by using a controller that manipulates the pulling rate and the chamber temperature to maintain these variables constant and allows neglecting the detailed dynamics of the crystal/melt interface in our analysis (see also remark 9) and discussion in the appendix); (b) the temperature distribution inside the crystal is assumed to be axisymmetric owing to the constant rotation of the crucible; (c) radiation is assumed to be the dominant heat-transfer mechanism; this assumption is justified from the fact that the temperatures of the chamber, melt and crystal surfaces are very high (1,000–1,700 K); (d) secondary radiation is not taken into account since it has a smaller effect on the crystal temperature profile compared to the primary radiation and the temperatures of the surrounding surfaces are kept constant at the desired set points using control; (e) the melt and chamber temperature and the pulling rate are assumed to be constant and the melt/crystal interface is assumed to be flat; this allows us to neglect the melt dynamics; (f) the solidification front remains in a specified region of the heater as the melt level drops; this is achieved in practice by raising the crucible through movement of the pedestal (Derby and Brown, 1986a); (g) the concentration of dopant, oxygen and carbon are not explicitly included in the model; this is done to simplify the controller synthesis task and special consideration is taken in the tuning of the controller (see subsection on nonlinear controller synthesis-closed-loop simulations) to ensure that large and abrupt heater temperature (manipulated input) changes, which could cause large variations in the concentration fields, do not occur.

Under these assumptions, an application of an energy balance to a differential element of the crystal yields the following two-dimensional (2-D) parabolic PDE

$$\frac{\partial T_c}{\partial t} + v_p \frac{\partial T_c}{\partial z} = \frac{k}{\rho c_p}\left[\frac{1}{r}\frac{\partial}{\partial r}\left(r\frac{\partial T_c}{\partial r}\right) + \frac{\partial^2 T_c}{\partial z^2}\right] \tag{1}$$

subject to the following boundary conditions

$$T_c(r,0,t) = T_{mp}, \quad 0 \le r \le R \tag{2}$$

$$\left.\frac{\partial T_c}{\partial r}\right|_0 = 0, \quad 0 \le z \le l(t) \tag{3}$$

$$\begin{aligned}\left.\frac{k}{\sigma}\frac{\partial T_c}{\partial r}\right|_R &= \epsilon_{w_{cr}}\epsilon_{w_m}F_{cr\to m}(R,z)\left[T_m^4 - T_c^4(R,z,t)\right] \\ &+ \epsilon_{w_{cr}}\epsilon_{w_{ch}}F_{cr\to ch}(R,z)\left[T_{ch}^4 - T_c^4(R,z,t)\right] \\ &+ \epsilon_{w_{cr}}\epsilon_{w_{amb}}F_{cr\to amb}(R,z)\left[T_{amb}^4 - T_c^4(R,z,t)\right], 0 \le z \le l(t)\end{aligned} \tag{4}$$

Table 1. Physical Properties of Si

Melting point	T_{mp}	1,683	K
Crystal specific heat	c_p	1,000	$J \cdot kg^{-1} \cdot K^{-1}$
Crystal density	ρ	2,420	$kg \cdot m^{-3}$
Crystal thermal conductivity	k	22	$J (s \cdot m \cdot K)^{-1}$
Crsytal emissivity	$\epsilon_{w_{cr}}$	0.7	
Melt emissivity	ϵ_{w_m}	0.7	

Table 2. Process Parameters

Chamber height	h_{ch}	0.18	m
Chamber radius	R_{ch}	0.15	m
Chamber emissivity	$\epsilon_{w_{ch}}$	0.3	
Chamber wall temp.	T_{ch}	1,500	K
Pulling velocity	v_p	1.66×10^{-5}	$m\,s^{-1}$
Melt temp.	T_m	1,705	K
Initial length of crystal	l_0	0.05	m
Final length of crystal	l_f	0.70	m
Radius of crystal	R	0.05	m
Ambient emissivity	$\epsilon_{w_{ch}}$	0.3	
Ambient temp.	T_{amb}	600	K
Ref. temp. for ith heater	T_{sp_i}	1,000	K

$$\frac{k}{\sigma}\frac{\partial T_c}{\partial z}\bigg|_{l(t)} = \epsilon_{w_{cr}}\epsilon_{w_m}F_{cr\to m}[r,l(t)]\{T_m^4 - T_c^4[r,l(t),t]\}$$

$$+ \epsilon_{w_{cr}}\epsilon_{w_{ch}}F_{cr\to ch}[r,l(t)]\{T_{ch}^4 - T_c^4[r,l(t),t]\}$$

$$+ \epsilon_{w_{cr}}\epsilon_{w_{\text{amb}}}F_{cr\to \text{amb}}[r,l(t)]\{T_{\text{amb}}^4 - T_c^4[r,l(t),t]\}, \quad 0 \le r \le R \tag{5}$$

In the above equations, T_c is the temperature of the crystal, t is the time, r is the radial direction, z is the axial direction, v_p is the pulling sped, T_{ch} is the chamber temperature, T_{amb} is the ambient temperature, T_{mp} is the melting point temperature of silicon, T_m is the temperature of the melt, σ is the Stefan-Boltzmann constant, $\epsilon_{w_{cr}}$, ϵ_{w_m}, $\epsilon_{w_{ch}}$, $\epsilon_{w_{\text{amb}}}$ denote the emissivities of the crystal, melt, chamber and ambient respectively, $F_{cr\to j}$ is the view factor from the surface of a differential element of the crystal, cr, to surface j, and $l(t)$ is the total height of the crystal at time t. The model of Eqs. 1–5 constitutes a parabolic PDE system with moving boundary owing to the variation of the length $l(t)$ of the crystal in the axial direction $l(t) = \int_0^t v_p(s)ds$, where $v_p(t)$ is the pulling rate.

In Eq. 1, the terms $\partial T_c/\partial t$ and $v_p\ (\partial T_c/\partial z)$ describe the rate of change of crystal temperature and the convection effect due to the motion of the crystal, respectively, while the terms $k/\rho c_p\ \{(1/r)\ (\partial/\partial r)\ [r(\partial T_c/\partial r)] + (\partial^2 T_c/\partial z^2)\}$ account for heat conduction inside the crystal. On the other hand, the boundary condition of Eq. 2 states that the crystal temperature in the crystal/melt interface is equal to the *Si* melting point temperature and the boundary condition of Eq. 3 is based on the assumption of axisymmetric crystal. Furthermore, the boundary condition of Eq. 4 accounts for radiative heat exchange between the *differential surface at the side of the crystal* and melt (term $\epsilon_{w_{cr}}\epsilon_{w_m}f_{cr\to m}(R,z)\ [T_m^4 - T_c^4(R,z,t)]$), chamber (term $\epsilon_{w_{cr}}\epsilon_{w_{ch}}F_{cr\to ch}(R,z)\ [T_{ch}^4 - T_c^4(R,z,t)]$) and ambient (term $\epsilon_{w_{cr}}\epsilon_{w_{\text{amb}}}F_{cr\to \text{amb}}(R,z)[T_{\text{amb}}^4 - T_c^4(R,z,t)]$), and the boundary condition of Eq. 5 accounts for radiative heat exchange between the *differential surface at the top of the crystal* and melt (term $\epsilon_{w_{cr}}\epsilon_{w_m}F_{cr\to m}[r,l(t)]\ \{T_m^4 - T_c^4[r,l(t),t]\}$, chamber (term $\epsilon_{w_{cr}}\epsilon_{w_{ch}}F_{cr\to ch}[r,l(t)]\ \{T_{ch}^4 - T_c^4[r,l(t),t]\}$ and ambient (term $\epsilon_{w_{cr}}\epsilon_{w_{\text{amb}}}F_{cr\to \text{amb}}[r,l(t)]\ \{T_{\text{amb}}^4 - T_c^4[r,l(t),t]\}$). The computation of the various view factors through decomposition of the corresponding complex geometries into simple geometries for which view factors can be computed analytically is discussed in the appendix.

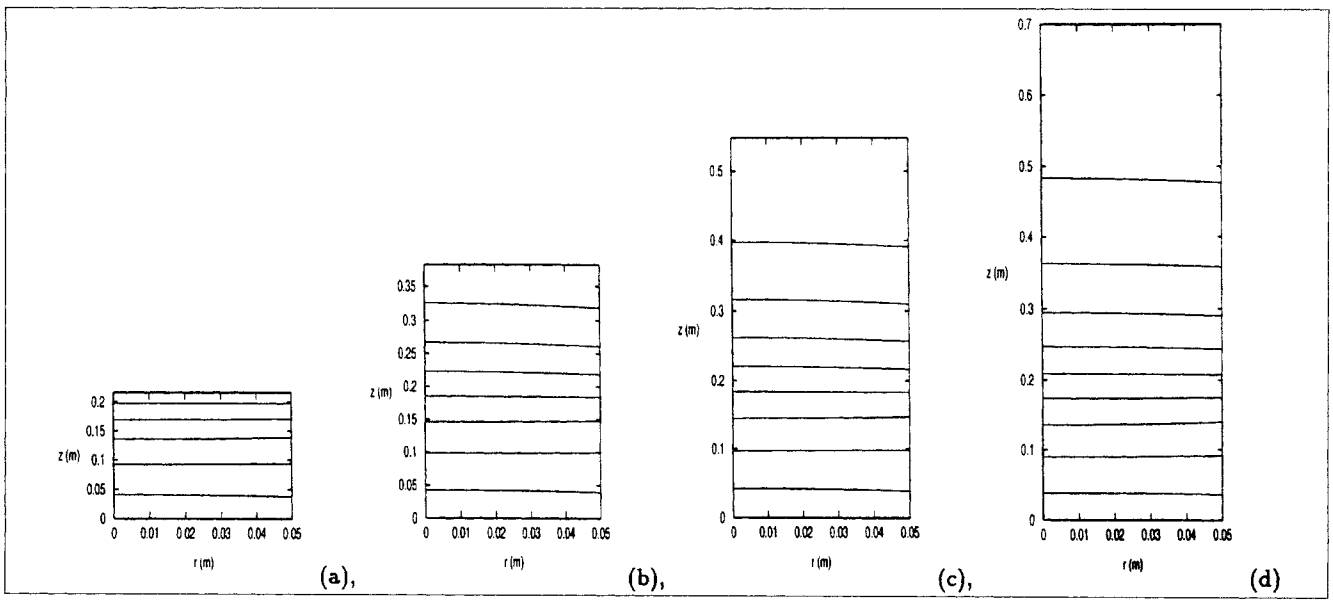

Figure 2. Temperature of crystal as a function of radial and axial coordinates for $T_{\text{amb}} = 600$ K.

(a) $t = 1 \times 10^4$ s; (b) $t = 2 \times 10^4$ s; (c) $t = 3 \times 10^4$ s; (d) $t = 4 \times 10^4$ s. Each contour represents a 100 K temperature difference.

Finally, the values of the physical properties of Si are given in Table 1, and the values of the parameters of the process are given in Table 2. We note that: (a) the Si crystal properties are assumed to be independent of the temperature and concentrations of dopant, carbon and oxygen, and (b) even though our study does not focus on a specific experimental or industrial Czochralski crystallizer, the values of the process parameters in Table 2 are within the range of values normally employed in industrial crystallizers (compare with the values given in Derby and Brown (1987)).

Remark 1: Regarding the development of the above model, we must note that the focus of our control effort is on the reduction of the magnitude of the thermal gradients inside the body of the crystal and thus we focus on the development of a model that describes the spatiotemporal evolution of the crystal temperature, once the crystal radius has obtained its final value, and accounts for the interactions (radiative heat transfer) between the crystal and its surroundings. There is an extensive literature on the development of integrated (global) models for the Czochralski process that include the crystal-melt interface shape and melt temperature dynamics (see, for example, Derby and Brown, 1986a,b, 1987; Zhou et al., 1994 for details). We finally note that the technique for order reduction and controller design that is presented in the next section can also be applied to these integrated crystal growth models to design controllers for crystal temperature regulation, but such an application is outside the scope of this work.

Control-Relevant Analysis of the Czochralski Crystal Growth

The objective of this section is to study the thermal gradients inside the crystal in the Czochralski crystal growth process to obtain insights which will be used to formulate a meaningful control problem and derive an appropriate model for controller synthesis. The mathematical model of the Czochralski crystal growth process of Figure 1 consisting of the 2-D parabolic PDE of Eq. 1 and the boundary conditions of Eqs. 2–5 was solved using Galerkin's method. Specifically, 30 global eigenfunctions (that is, trigonometric functions that cover the entire domain) in the axial direction and 30 global (Bessel) eigenfunctions in the radial direction were used as basis functions in Galerkin's method to discretize the process model in space and reduce it into a large set (900 equations) of ODEs. The time-integration of the large set of ODEs was

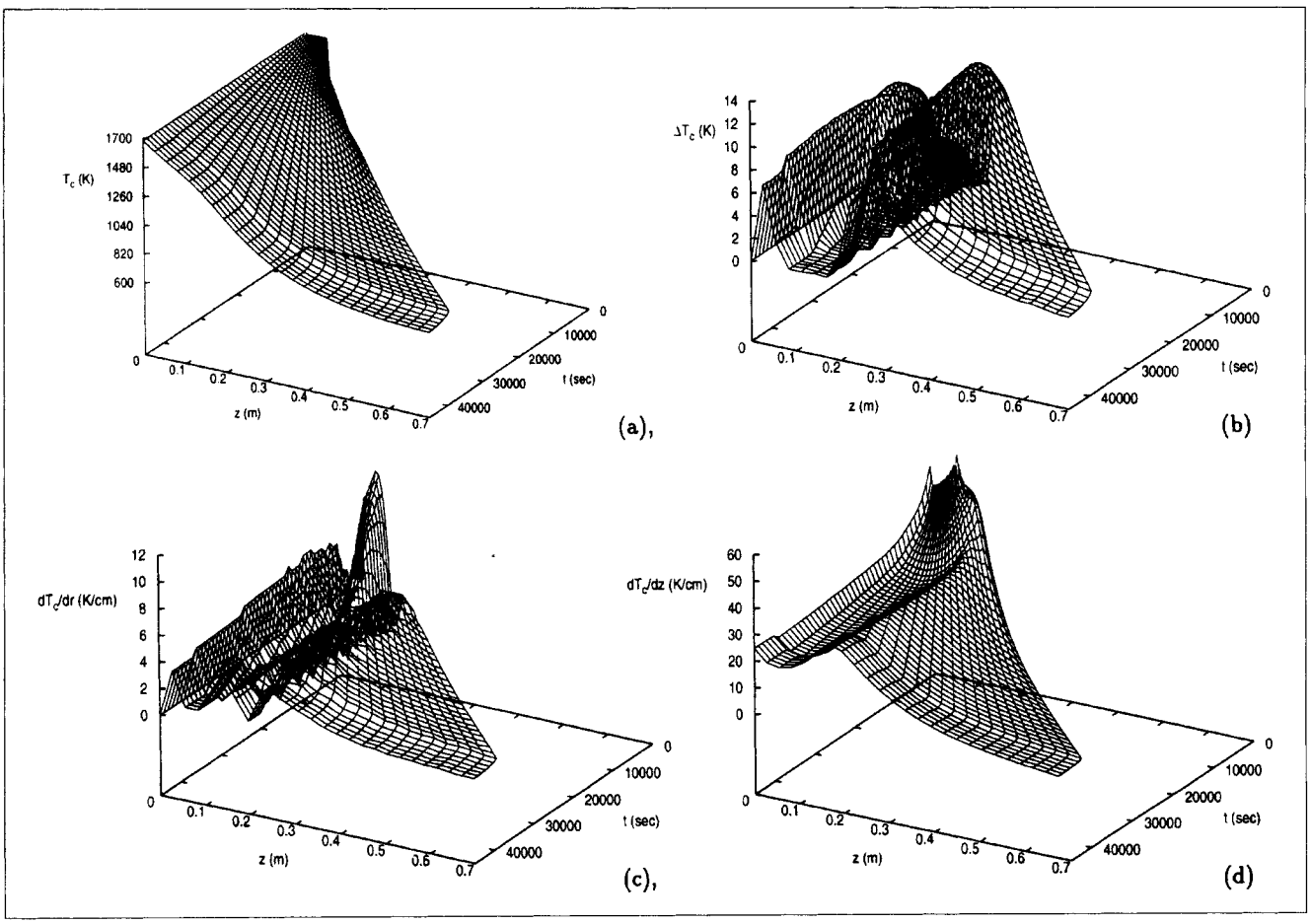

Figure 3. (a) Temperature of crystal at $r = 0.0$ m; (b) maximum temperature difference inside the crystal in the radial direction; (c) maximum thermal gradient inside the crystal in the radial direction; (d) maximum thermal gradient inside the crystal in the axial direction, as a function of time and axial coordinate for $T_{amb} = 600$ K.

performed utilizing explicit Euler. It was verified that further increase in the number of eigenfunctions in both r and z directions, as well as reduction in the step of time-integration, results in negligible change in the accuracy of the computed solution. In all the simulation runs, the crystal is initially assumed to be at $l(0) = 0.05\ m$ and $T_c(r, z, 0) = 1{,}670$ K.

Figures 2 and 3a show the contour plots of the crystal temperature as a function of the axial and radial directions at four different time instants during the operation of the process and the temporal evolution of the crystal temperature in the axial direction at the center of the crystal, respectively, when the temperature of the ambient (void space in the furnace surrounding the crystal) is set at $T_{\text{amb}} = 600$ K. We observe that the temperature drop inside the crystal in the axial direction is much larger (almost 700 K) than the temperature drop inside the crystal in the radial direction (less than 20 K; see also Figure 3b). This can also be seen in Figures 3c and 3d that show the maximum thermal gradient in the radial and axial direction, respectively, as a function of the axial parameter and time. We observe that the maximum thermal gradient in the axial direction is 5 times larger than the maximum thermal gradient in the radial direction, for all times.

To further investigate this observation, we will show in Figures 5 and 7 the temporal evolution of the crystal temperature when the temperature of the ambient is set at $T_{\text{amb}} =$ 1,000 K and $T_{\text{amb}} = 1{,}400$ K, respectively. Again, it is clear that the variation of the crystal temperature in the radial direction is negligible compared to the variation in the axial one. This can also be seen in Figures 4 and 6 presenting contour plots of the crystal temperature, when the ambient temperature is $T_{\text{amb}} = 1{,}000$ K and $T_{\text{amb}} = 1{,}400$ K, respectively. This conclusion is very important because it allows neglecting the radial dependence of the crystal temperature in the process model which will be used as the basis for the synthesis of a nonlinear feedback controller, thereby yielding the following 1-D parabolic PDE with moving boundary

$$\frac{\partial T_c}{\partial t} + v_p \frac{\partial T_c}{\partial z} = \frac{k}{\rho c_p} \frac{\partial^2 T_c}{\partial z^2} + \frac{2\sigma \epsilon_{w_{cr}} \epsilon_{w_m}}{\rho c_p R} \times F_{cr \to m}(R, z)\left[T_m^4 - T_c^4(z,t)\right] + \frac{2\sigma \epsilon_{w_{cr}} \epsilon_{w_{ch}}}{\rho c_p R} F_{cr \to ch}(R, z)\left[T_{ch}^4 - T_c^4(z,t)\right] + \frac{2\sigma \epsilon_{w_{cr}} \epsilon_{w_{\text{amb}}}}{\rho c_p R} F_{\text{cr} \to \text{amb}}(R, z)\left[T_{\text{amb}}^4 - T_c^4(z,t)\right] \quad (6)$$

subject to the boundary conditions

$$T_c(0,t) = T_{mp} \quad (7)$$

$$\frac{k}{\sigma} \frac{\partial T_c}{\partial z}\bigg|_{l(t)} = \epsilon_{w_{cr}} \epsilon_{w_m} F_{cr \to m}[l(t)]\{T_m^4 - T_c^4[l(t),t]\} + \epsilon_{w_{cr}} \epsilon_{w_{ch}} F_{cr \to ch}[l(t)]\{T_{ch}^4 - T_c^4[l(t),t]\} + \epsilon_{w_{cr}} \epsilon_{w_{\text{amb}}} F_{cr \to \text{amb}}[l(t)]\{T_{\text{amb}}^4 - T_c^4[l(t),t]\} \quad (8)$$

An additional conclusion which follows from the study of Figures 3, 5 and 7 is that the ambient temperature T_{amb} has a very significant effect on the axial profile of the crystal temperature. This suggests that T_{amb} is a meaningful choice for a manipulated variable in order to enforce a desired temperature drop inside the crystal. Therefore, we formulate the con-

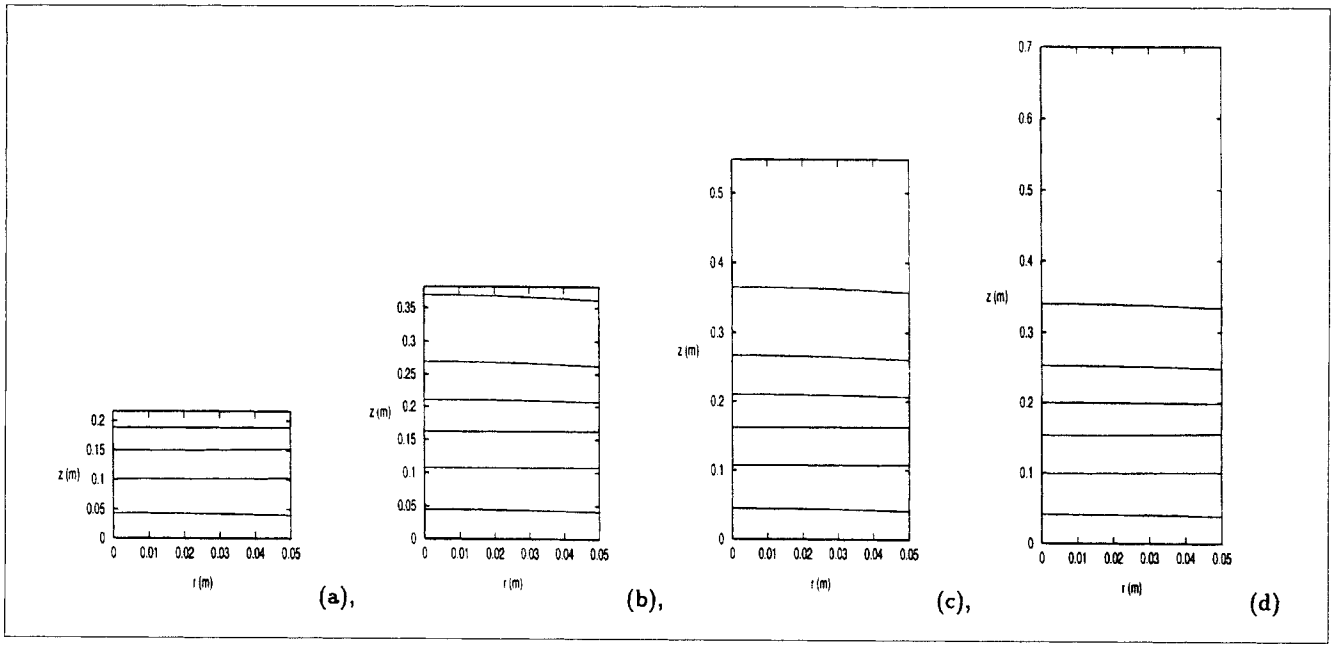

Figure 4. Temperature of crystal as a function of radial and axial coordinates for $T_{\text{amb}} = 1{,}000$ K.

(a) $t = 1 \times 10^4$ s; (b) $t = 2 \times 10^4$ s; (c) $t = 3 \times 10^4$ s (d) $t = 4 \times 10^4$ s. Each contour represents a 100 K temperature difference.

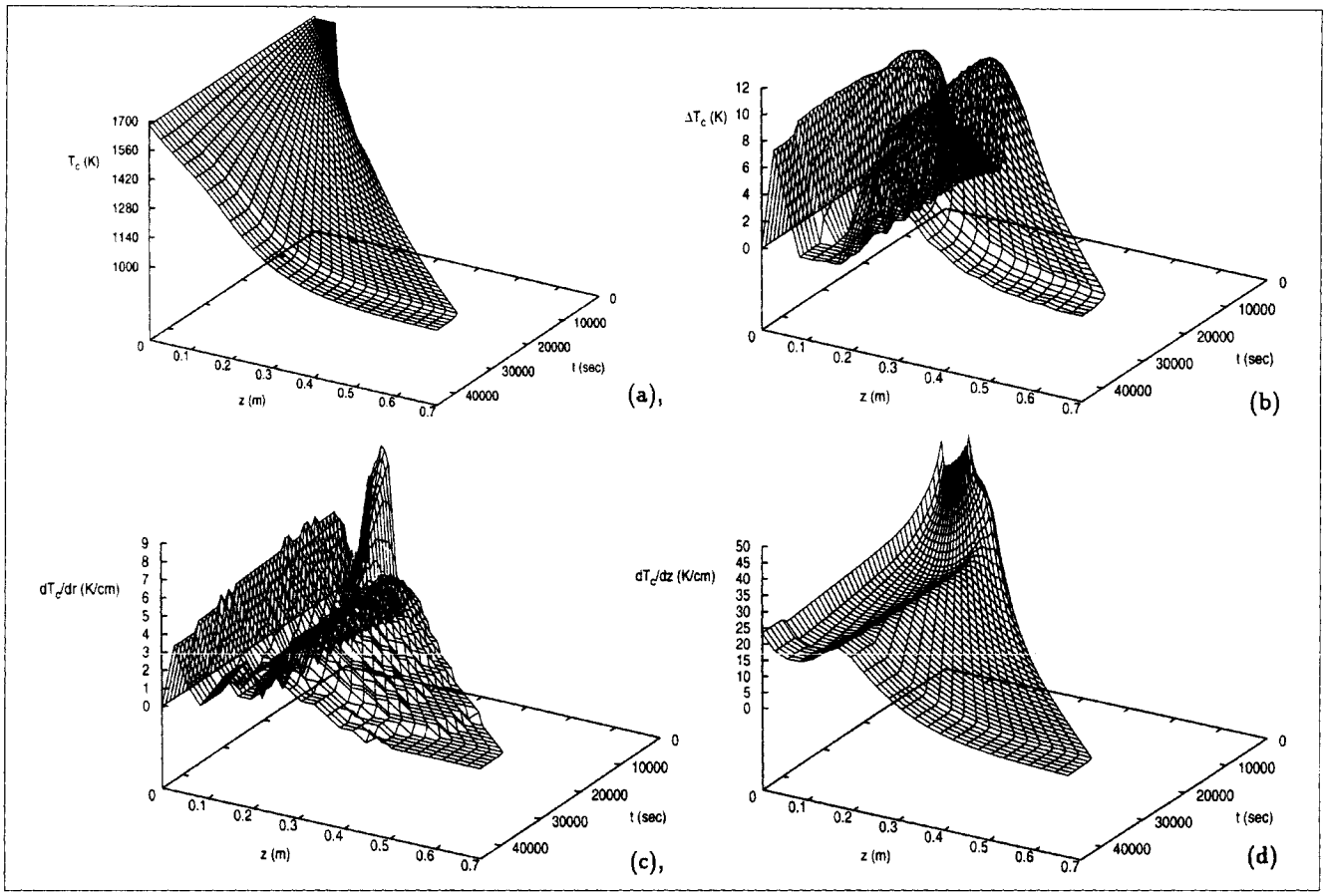

Figure 5. (a) Temperature of crystal at $r = 0.0$ m; (b) maximum temperature difference inside the crystal in the radial direction; (c) maximum thermal gradient inside the crystal in the radial direction; (d) maximum thermal gradient inside the crystal in the axial direction, as a function of time and axial coordinate for $T_{amb} = 1{,}000$ K.

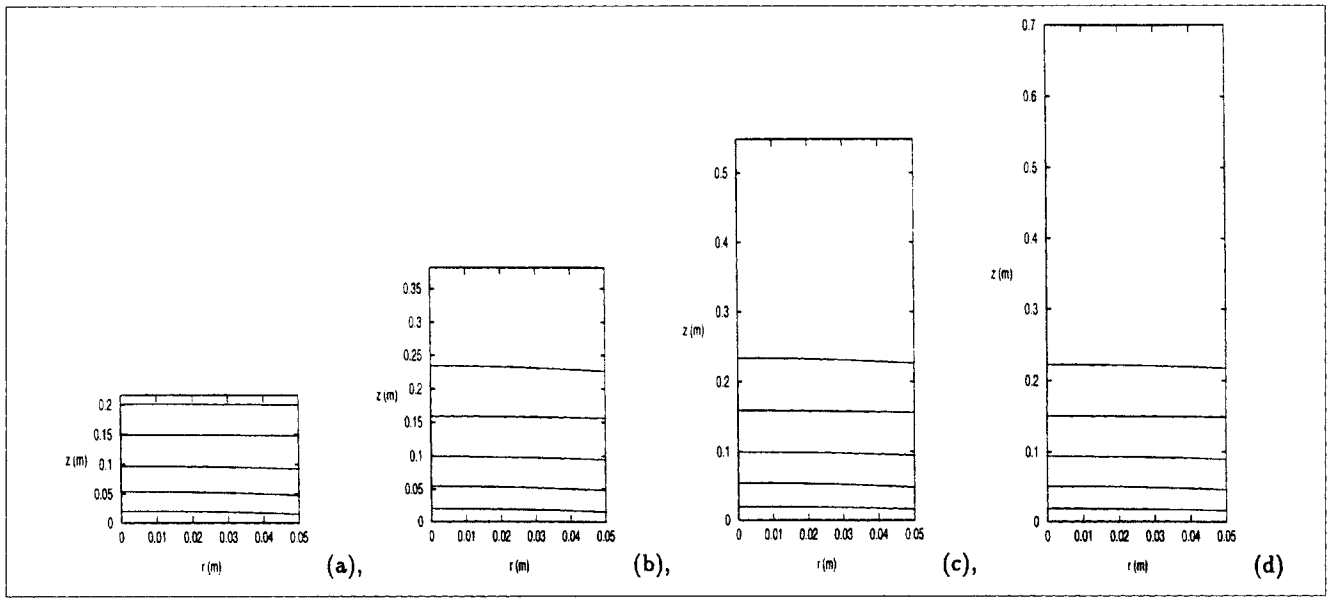

Figure 6. Temperature of crystal as a function of radial and axial coordinates for $T_{amb} = 1{,}400$ K.

(a) $t = 1 \times 10^4$ s; (b) $t = 2 \times 10^4$ s; (c) $t = 3 \times 10^4$ s; (d) $t = 4 \times 10^4$ s. Each contour represents a 50 K temperature difference.

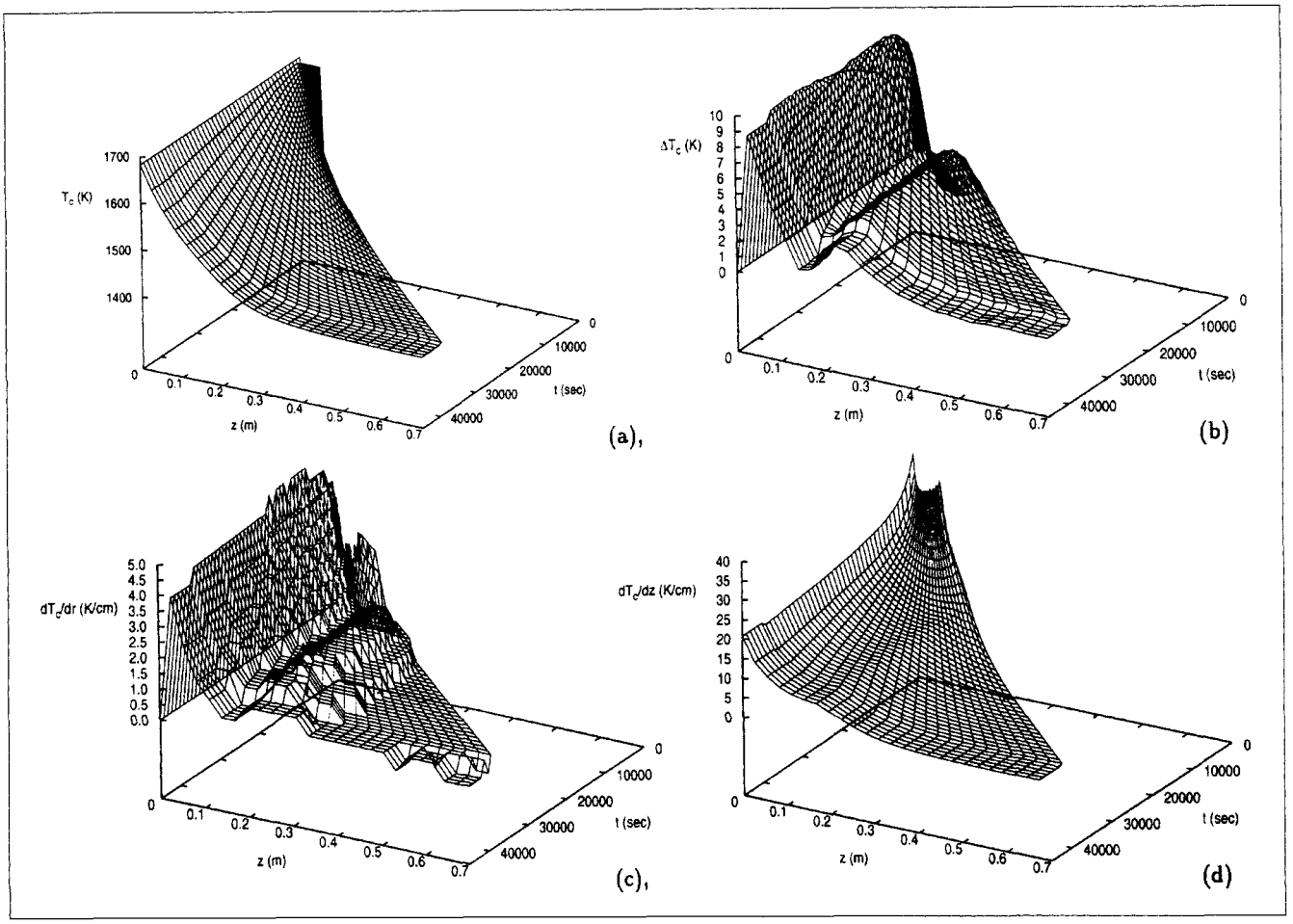

Figure 7. (a) Temperature of crystal at $r = 0.0$ m; (b) maximum temperature difference inside the crystal in the radial direction; (c) maximum thermal gradient inside the crystal in the radial direction; (d) maximum thermal gradient inside the crystal in the axial direction, as a function of time and axial coordinate for $T_{amb} = 1{,}400$ K.

trol problem as the one of controlling the temperature gradient of the crystal in the axial direction by manipulating the temperature of extra heaters placed above the chamber at equispaced intervals. The use of extra heaters to control the crystal temperature is also motivated by the realization that the regulation of thermal gradients in the axial direction requires the use of a manipulated variable which is distributed along the length of the crystal. We will show later on that the use of extra heaters to control axial thermal gradients will also lead to significant reduction of the radial thermal gradients inside the crystal (which cannot be directly controlled) owing to the well-regulated thermal environment in which the crystal grows in such a case.

Our attention now turns to the development of the control configuration that will be used to regulate the thermal gradients inside the crystal; this entails the computation of the number of separate components of the heaters needed to achieve the desired regulation of the thermal gradients. To this end, we initially assumed that the temperature of the heaters is spatially uniform and used a single proportional integral controller to manipulate this temperature of the form

$$\dot{\xi} = y_{sp} - y, \xi(0) = 0$$
$$u = K(y_{sp} - y) + \frac{1}{\tau}\xi \tag{9}$$

The objective of the controller was to keep the surface temperature of the crystal at position $z = 0.48$ m at a constant value of 1,250 K, and enforce a smooth temperature inside the crystal, below the critical value of 20 K/cm (Gevelber, 1994a). The parameters of the controller are given in Table 3.

Figure 8a will show the temporal evolution of the temperature at the center of the crystal in the axial direction in the closed-loop system. Clearly, the controller drives the temperature of the crystal to its new set point, and the temperature gradients in the radial direction remain small for almost all times (see Figure 8c and compare with 3c). However, the controller fails to establish a smooth temperature drop inside the crystal in the axial direction, enforcing a large temperature drop close to the crystal-melt interface and achieving an almost uniform crystal temperature far away from the inter-

Table 3. PI Control Parameters

z_s [m]	z_f [m]	z_m [m]	K	τ	T_s [K]
0.18	0.71	0.48	3	1.0	1,250

face; this can be seen in Figure 9 which shows the contour plots of the crystal temperature as a function of the axial and radial directions at four different time instants during the operation of the process. Figure 10 shows the corresponding profile for the manipulated input, which changes smoothly with time to achieve the control objective (the initial sharp change of the manipulated input is actually a smooth change which occurs over a time period of 250 s and is due to the fact that the time axis covers the entire process cycle). Note that the controller is activated [that is, $u(t) \neq 1$] when the crystal enters in the zone in which the control actuator operates. Regarding Figure 8, it is worth noting that the radial temperature nonuniformity remains small (less than 10 K) for the whole process time, which further validates the conclusion that we have drawn on the basis of the open-loop behavior that radial thermal gradients are much smaller than axial thermal gradients (see also last paragraph in the subsection on nonlinear controller synthesis-closed-loop simulations for more discussion on this issue).

Based on the simulation results for the case of using a single control actuator and driven by our desire to achieve a smooth temperature drop inside the crystal, we formulate the control problem as the one of controlling the temperature gradient of the crystal in the axial direction by manipulating the temperature of three extra heaters placed at three equispaced intervals, as shown in Figure 11. To account for the heaters used for crystal temperature control in the 2-D process model, we substitute the boundary conditions of Eqs. 4 and 5 with the following boundary conditions

$$\frac{k}{\sigma}\frac{\partial T_c}{\partial r}\bigg|_R = \epsilon_{w_{cr}}\epsilon_{w_m}F_{cr\to m}(R,z)\left[T_m^4 - T_c^4(R,z,t)\right] + \epsilon_{w_{cr}}\epsilon_{w_{ch}}F_{cr\to ch}(R,z)\left[T_{ch}^4 - T_c^4(R,z,t)\right] + \epsilon_{w_{cr}}\sum_{i=1}^{3}\epsilon_{w_i}F_{cr\to i}(R,z)\left[T_i^4(t) - T_c^4(R,z,t)\right], \quad 0 \le z \le l(t) \quad (10)$$

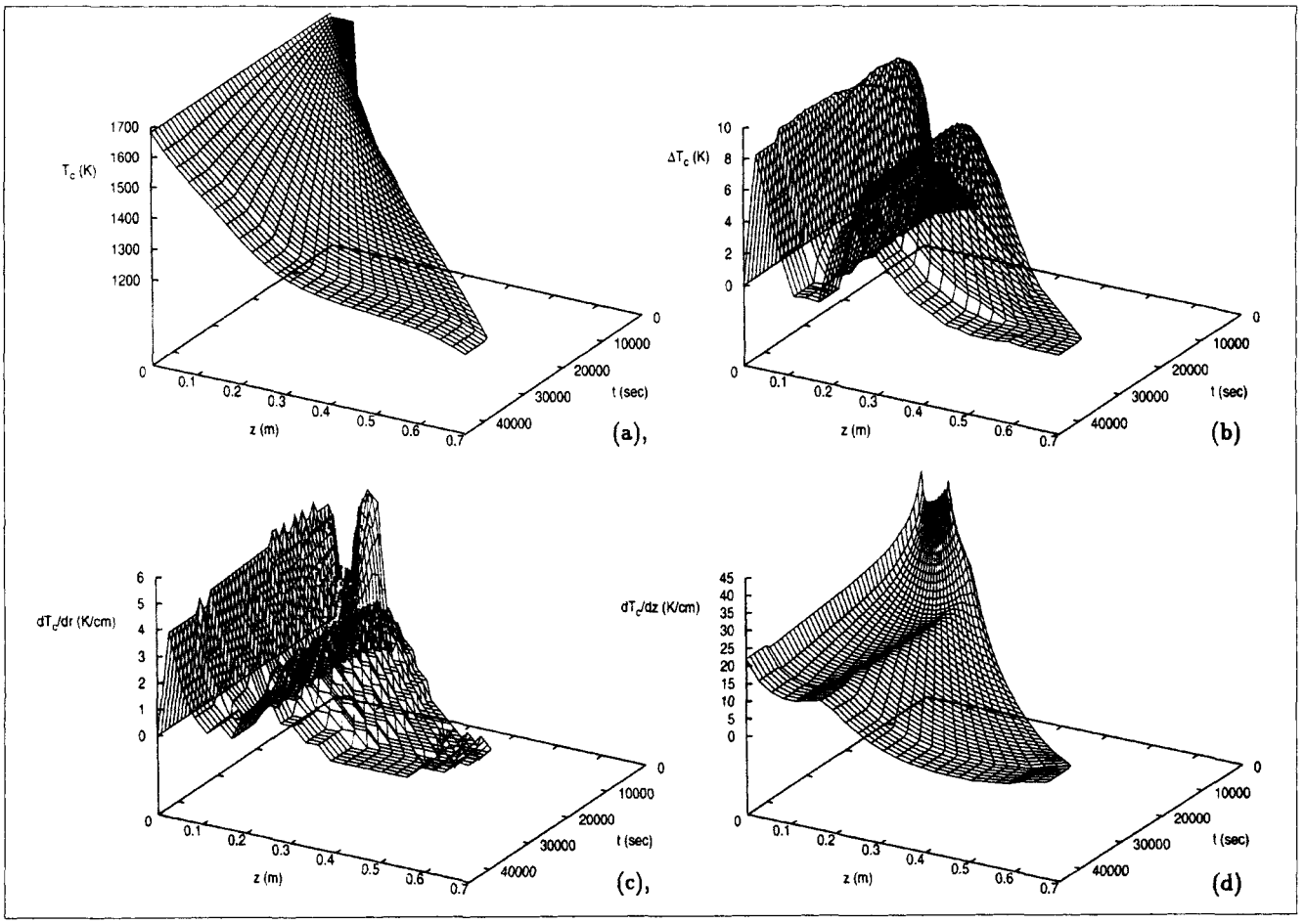

Figure 8. (a) Temperature of crystal at $r = 0.0$ m; (b) maximum temperature difference inside the crystal in the radial direction; (c) maximum thermal gradient inside the crystal in the radial direction; (d) maximum thermal gradient inside the crystal in the axial direction, as a function of time and axial coordinate-one PI controller.

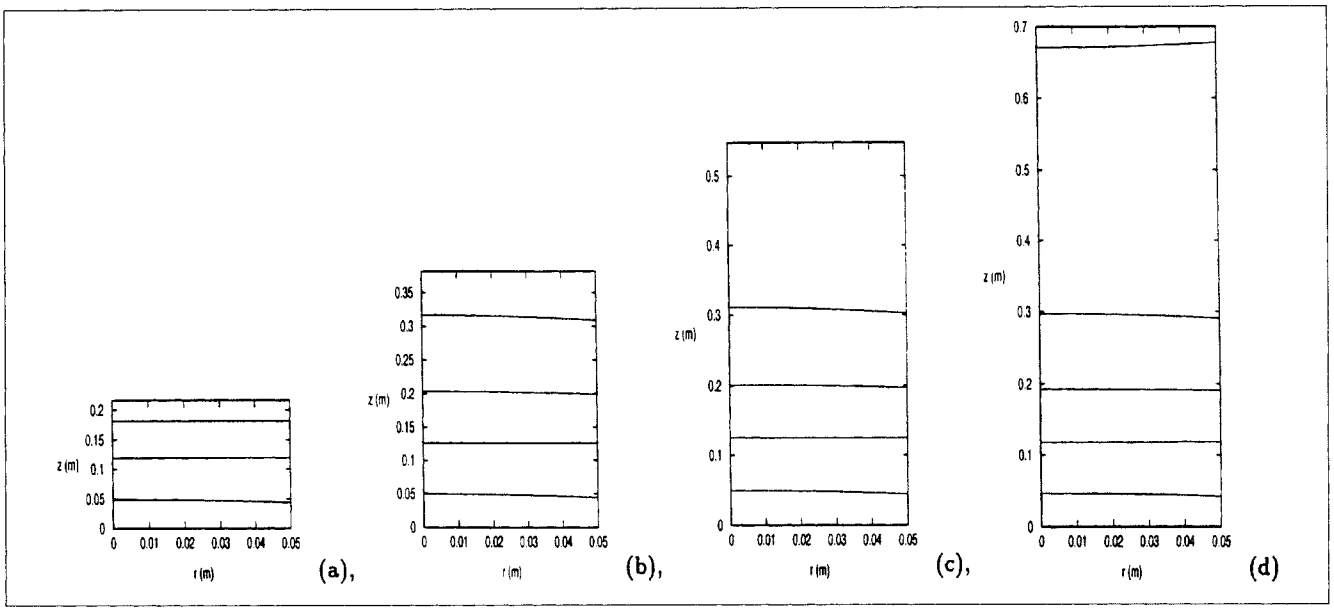

Figure 9. Temperature of crystal as a function of radial and axial coordinates-one PI controller.

(a) $t = 1\times10^4$ s; (b) $t = 2\times10^4$ s; (c) $t = 3\times10^4$ s; (d) $t = 4\times10^4$ s. Each contour represents a 100 K temperature difference.

$$\left.\frac{k}{\sigma}\frac{\partial T_c}{\partial z}\right|_{l(t)} = \epsilon_{w_{cr}}\epsilon_{w_m}F_{cr\to m}[r,l(t)]\left[T_m^4 - T_c^4(r,l(t),t)\right] + \epsilon_{wcr}\epsilon_{w_{ch}}F_{cr\to ch}[r,l(t)]\left[T_{ch}^4 - T_c^4(r,l(t),t)\right] + \epsilon_{w_{cr}}\sum_{i=1}^{3}\epsilon_{w_i}F_{cr\to i}[r,l(t)]\left[T_i^4(t) - T_c^4(r,l(t),t)\right], \quad 0\le r\le R \quad (11)$$

where n is the number of heaters used for control, $T_i(t)$ is the temperature of the i-th heater, and $F_{cr\to i}$ is the view factor of a differential crystal surface element to the heater surface.

Moreover, with the addition of the heaters, the 1-D model which will be used for controller design takes the form

$$\frac{\partial T_c}{\partial t} + v_p\frac{\partial T_c}{\partial z} = \frac{k}{\rho c_p}\frac{\partial^2 T_c}{\partial z^2} + \frac{2\sigma\epsilon_{w_{cr}}\epsilon_{w_m}}{\rho c_p R}F_{cr\to m}(R,z)\left[T_m^4 - T_c^4(z,t)\right] + \frac{2\sigma\epsilon_{w_{cr}}\epsilon_{w_{ch}}}{\rho c_p R}F_{cr\to ch}(R,z)\left[T_{ch}^4 - T_c^4(z,t)\right] + \frac{2\sigma\epsilon_{w_{cr}}}{\rho c_p R}\sum_{i=1}^{3}\epsilon_{w_i}F_{cr\to i}(R,z)\left[T_i^4(t) - T_c^4(z,t)\right] \quad (12)$$

subject to the following boundary conditions

$$T_c(0,t) = T_{mp}$$

$$\left.\frac{k}{\sigma}\frac{\partial T_c}{\partial z}\right|_{l(t)} = \epsilon_{w_{cr}}\epsilon_{w_m}F_{cr\to m}[l(t)]\left[T_m^4 - T_c^4(l(t),t)\right] + \epsilon_{w_{cr}}\epsilon_{w_{ch}}F_{cr\to ch}[l(t)]\left[T_{ch}^4 - T_c^4(l(t),t)\right] + \epsilon_{w_{cr}}\sum_{i=1}^{3}\epsilon_{w_i}F_{cr\to i}[l(t)]\left[T_i^4(t) - T_c^4(l(t),t)\right] \quad (13)$$

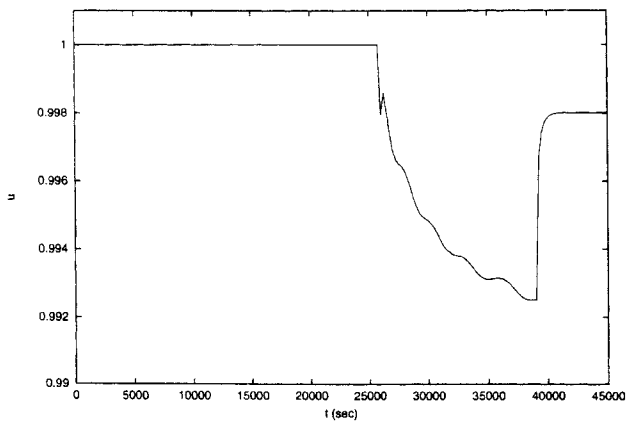

Figure 10. Manipulated input profile-PI controller.

Referring to Eqs. 12–13, note the lack of the terms corresponding to heat transfer between the crystal and the ambient (compare with Eqs. 6–8); these terms have been substituted by the terms that account for heat transfer between the crystal and the extra heaters that are used as control actuators.

The performance of the proposed control configuration that employs three heaters to regulate the thermal gradients inside the crystal compared to the open-loop system and the

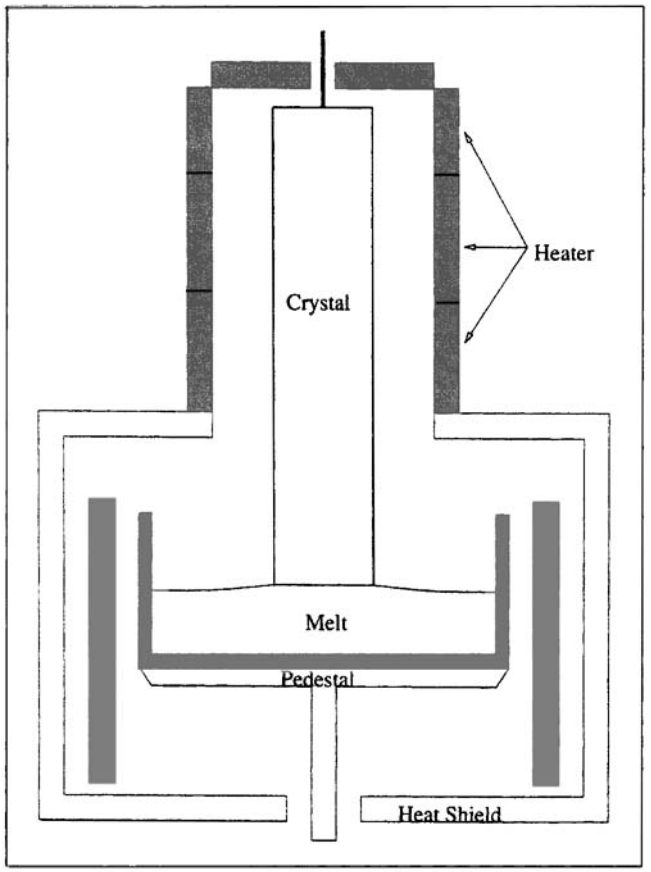

Figure 11. Control configuration for crystal temperature control in the Czochralski crystal growth.

closed-loop system in the case of using one heater will be evaluated later.

Remark 2: We note that another approach for the simulation of the crystal temperature concerns the elimination of the thermal dynamics of the process on the basis that they are slower than the dynamics of the crystal radius, and solves for the temperature profile inside the growing crystal as a series of solutions of a steady-state thermal model for different lengths (see, for example, Derby and Brown (1987, 1988)). However, in the present study, we have decided to include the thermal dynamics in the model of the process which is used for the implementation of the controller, because the use of feedback control or the presence of disturbances (for example, variations in the pulling rate, melt temperature) may significantly modify the dynamic behavior of the process compared to the open-loop behavior.

Nonlinear Model Reduction and Control of Processes with Moving Domains

Preliminaries

In this section, we present the theoretical results needed for the synthesis of a low-order nonlinear controller for the CZ processes based on the 1-D model of Eqs. 12–13. To this end, we use the following general state-space description of the model of Eqs. 12–13.

$$\frac{\partial \bar{x}}{\partial t} = A\frac{\partial \bar{x}}{\partial z} + B\frac{\partial^2 \bar{x}}{\partial z^2} + wb(z,t)u + f(z,t,\bar{x})$$

$$y_{c_i} = \int_0^{l(t)} c_i(z,t)k\bar{x}dz, \quad i = 1,\ldots,l \tag{14}$$

$$y_{m_\kappa} = \int_0^{l(t)} s_\kappa(z,t)\omega\bar{x}dz, \quad \kappa = 1,\ldots,q$$

subject to the boundary conditions

$$C_1\bar{x}(0,t) + D_1\frac{\partial \bar{x}}{\partial z}(0,t) = R_1$$

$$C_2\bar{x}(l(t),t) + D_2\frac{\partial \bar{x}}{\partial z}(l(t),t) = R_2 \tag{15}$$

and the initial condition

$$\bar{x}(z,0) = \bar{x}_0(z) \tag{16}$$

where $\bar{x}(z,t)][\bar{x}_1(z,t)\ldots\bar{x}_n(z,t)]^T$ denotes the vector of state variables, $[0,l(t)]\subset\mathbb{R}$ is the domain of definition of the process, $z\in[0,l(t)]$ is the spatial coordinate, $t\in[0,\infty)$ is the time, $u=[u_1u_2\ldots u_1]^T\in\mathbb{R}^l$ denotes the vector of manipulated inputs, $y_{c_i}\in\mathbb{R}$ denotes the i-th controlled output, $y_{m_\kappa}\in\mathbb{R}$ denotes the κ-th measured output $f(t,\bar{x})$ is a nonlinear vector function, k, w, ω are constant vectors, A, B, C_1, D_1, C_2,D_2 are constant matrices, R_1, R_2 are column vectors, and $\bar{x}_0(z)$ is the initial condition. $b(z,t)$ is a known smooth vector function of (z,t) of the form $b(z,t)=[b_1(z,t)b_2(z,t)\ldots b_l(z,t)]$, where $b_i(z,t)$ describes how the control action $u_i(t)$ is distributed in the interval $[0,l(t)]$ (such as point/distributed actuation), $c_i(z,t)$ is a known smooth function of (z,t) which is determined by the desired performance specifications in the interval $[0,l(t)]$ (such as regulation of the crystal temperature at a specific point or of a weighted average) and $s_\kappa(z,t)$ is a known smooth function of (z,t) which is determined by the location and type of the κ-th measurement sensor (such as point/distributed sensing). Finally, we point out that: (a) the length of the domain $l(t)$ is assumed to be a sufficiently smooth and bounded function of time which is also known (this assumption is certainly true for the crystal growth process where $l(t)$ is directly determined by the crystal pulling rate; $l(t)=\int_0^t v_p(s)ds$), and (b) the actuator, performance specification and measurement sensor distribution functions are allowed to depend explicitly on time (that is, moving control actuators and objectives, and measurement sensors).

In order to simplify the presentation of the model reduction and controller synthesis results, we formulate the system of Eqs. 14–16 in a Hilbert space $\mathcal{H}(t)$ consisting of n-dimensional vector functions defined on $[0,l(t)]$ that satisfy the boundary conditions of Eq. 15, with inner product and norm $(\omega_1,\omega_2)=\int_0^{l(t)}(\omega_1(z),\omega_2(z))_{\mathbb{R}}^n dz$, $\|\omega_1\|_2=(\omega_1,\omega_1)^{1/2}$ where ω_1, ω_2 are two elements of $\mathcal{H}(t)$ and the notation $(\cdot,\cdot)\mathbb{R}^n$ denotes the standard inner product in $\mathbb{R}^n$. To this end, we define the state function x on $\mathcal{H}(t)$ as

$$x(t) = \bar{x}(z,t), t>0, z\in[0,l(t)], \tag{17}$$

the time-varying operator

$$\mathfrak{A}(t)x = A\frac{\partial \bar{x}}{\partial z} + B\frac{\partial^2 \bar{x}}{\partial z^2} + \frac{i}{l(t)} \cdot z \cdot \frac{\partial \bar{x}}{\partial z},$$

$$x \in D(\mathfrak{A}) = \left\{ x \in \mathfrak{X}(t): \quad C_1 \bar{x}(0,t) + D_1 \frac{\partial \bar{x}}{\partial z}(0,t) \right.$$

$$\left. = R_1, C_2 \bar{x}[l(t),t] + D_2 \frac{\partial \bar{x}}{\partial z}[l(t),t] = R_2 \right\} \qquad (18)$$

and the input, controlled output and measurement operators as

$$\mathfrak{B}(t)u = wb(t)u, \mathfrak{C}(t)x = (c(t), kx), \mathfrak{S}(t)x = (s(t), \omega x) \qquad (19)$$

where $c(t) = [c_1(t)c_2(t)\ldots c_l(t)]$ and $s(t) = [s_1(t)s_2(t)\ldots s_q(t)]^T$ and $c_i(t) \in \mathfrak{X}(t)$, $s_\kappa(t) \in \mathfrak{X}(t)$. The system of Eqs. 14–16 can then be written as

$$\dot{x} = \mathfrak{A}(t)x + \mathfrak{B}(t)u + f(t,x), x(0) = x_0$$
$$y_c = \mathfrak{C}(t)x, y_m = \mathfrak{S}(t)x \qquad (20)$$

where $f[t, x(t)] = f[t, \bar{x}(z,t)]$ and $x_0 = \bar{x}_0(z)$. The system of Eq. 20 will be used in the next two subsections to present the model reduction and control algorithms that we apply to the crystal growth process. Our presentation will focus on the algorithms applied to the crystal growth process, and detailed proofs of approximation and controller synthesis results can be found in Armaou and Christofides (1999).

Nonlinear model reduction

In this section, we construct nonlinear low-dimensional ODE systems that accurately reproduce the dynamics and solutions of the infinite dimensional system of Eq. 22, which will be used for controller design. The construction of the ODE systems is achieved by using a nonlinear model reduction procedure which is based on a combination of standard Galerkin's method with the concept of approximate inertial manifold and exploits the fact that the eigenspectrum of $\mathfrak{A}(t)$ can be partitioned into a finite-dimensional part containing m slow eigenvalues and a stable infinite-dimensional complement containing the remaining fast eigenvalues.

We initially transform the system of Eq. 20 into a set of infinite ODEs. Let $\{\phi_j(t)\}$, $j = 1, \ldots, \infty$, be the set of eigenfunctions of $\mathfrak{A}(t)$; this is an orthogonal and countable set $\forall t \in [0, \infty)$, and forms a basis of $\mathfrak{X}(t)$. Let also $\mathfrak{X}_s(t) = \text{span}\{\phi_1(t), \phi_2(t), \ldots, \phi_m(t)\}$ and $\mathfrak{X}_f(t) = \text{span}\{\phi_{m+1}(t), \phi_{m+2}(t), \ldots,\}$ be two modal subspaces of $\mathfrak{X}(t)$ such that $\mathfrak{X}_s(t) \oplus \mathfrak{X}_f(t) = \mathfrak{X}(t)$. Note that $\mathfrak{X}_s(t)$ includes the eigenfunctions of $\mathfrak{A}(t)$ corresponding to the dominant (slow) eigenvalues, while $\mathfrak{X}_f(t)$ includes the eigenfunctions of $\mathfrak{A}(t)$ corresponding to the remaining fast eigenvalues. Defining the orthogonal (pointwise in time) projection operators $P_s: \mathfrak{X}(t) \to \mathfrak{X}_s(t)$ and $P_f: \mathfrak{X}(t) \to \mathfrak{X}_f(t)$ so that the state x of the system of Eq. 20 can be written as $x = x_s + x_f = P_s x + P_f x$, and applying P_s and P_f to the system of Eq. 20, we obtain

$$\frac{dx_s}{dt} = \mathfrak{A}_s(t)x_s + \mathfrak{B}_s(t)u + f_s(t, x_s, x_f), x_s(0) = P_s x_0$$

$$\frac{\partial x_f}{\partial t} = \mathfrak{A}_f(t)x_f + \mathfrak{B}_f(t)u + f_f(t, x_s, x_f), x_f(0) = P_f x_0$$

$$y_c = \mathfrak{C}(t)(x_s + x_f), y_m = \mathfrak{S}(t)(x_s + x_f) \qquad (21)$$

where $\mathfrak{A}_s(t) = P_s\,\mathfrak{A}(t)$, $\mathfrak{B}_s(t) = P_s\,\mathfrak{B}(t)$, $f_s(t, x_s, x_f) = P_s f(t,x)$, $\mathfrak{A}_f(t) = P_f\,\mathfrak{A}(t)$ is an unbounded differential operator, $\mathfrak{B}_f(t) = P_f\,\mathfrak{B}(t)$, and $f_f(t, x_s, x_f) = P_f f(t,x)$. To take advantage of the two-time-scale property of the spectrum of $\mathfrak{A}(t)$, we define

$$\epsilon = \sup_{t \in [0,\infty)} \frac{|Re\lambda_1(t)|}{|Re\lambda_{m+1}(t)|},$$

where $\lambda_1(t)$ is the largest eigenvalue of the matrix $\mathfrak{A}_s(t)$ and $\lambda_{m+1}(t)$ is the largest eigenvalue of the operator (infinite range matrix) $P_f\,\mathfrak{A}(t)$, and multiply the x_f-subsystem of Eq. 21 by ϵ, to obtain:

$$\frac{dx_s}{dt} = \mathfrak{A}_s(t)x_s + \mathfrak{B}_s(t)u + f_s(t, x_s, x_f), x_s(0) = P_s x_0$$

$$\epsilon\frac{\partial x_f}{\partial t} = \mathfrak{A}_{f\epsilon}(t)x_f + \epsilon\,\mathfrak{B}_f(t)u + \epsilon f_f(t, x_s, x_f), x_f(0) = P_f x_0$$

$$y_c = \mathfrak{C}(t)(x_s + x_f), y_m = \mathfrak{S}(t)(x_s + x_f) \qquad (22)$$

where $\mathfrak{A}_{f\epsilon}(t) = \epsilon P_f\,\mathfrak{A}(t)$ and the operators $\mathfrak{A}_s(t)$, $\mathfrak{A}_{f\epsilon}(t)$ generate semigroups with growth rates which are of the same order of magnitude. The subsystem which describes the fast dynamics of the system of Eq. 22 can be obtained by writing the system of Eq. 22 in the fast time scale $\tau = t/\epsilon$ and setting $\epsilon = 0$ and has the form

$$\frac{\partial x_f}{\partial \tau} = \mathfrak{A}_{f\epsilon}(t)x_f \qquad (23)$$

We choose $\mathfrak{X}_s(t)$ and $\mathfrak{X}_f(t)$ so that the above system is exponentially stable (note that this is always possible for parabolic PDE systems; see Armaou and Christofides (1999) for details).

The reduction of the system of infinite ODEs of Eq. 22 into a finite set of ODEs can be performed by using the concept of inertial manifold for systems with time-varying operators introduced in Armaou and Christofides (1999) (see also Jones and Titi (1994) for other concepts of IMs for infinite-dimensional systems with time-varying terms). Specifically, if exists, an inertial manifold $\mathfrak{M}(t)$ for the system of Eq. 22 is a subset of $\mathfrak{X}(t)$, which satisfies the following properties:

(i) $\mathfrak{M}(t)$ is a finite-dimensional Lipschitz manifold,

(ii) $\mathfrak{M}(t)$ is a graph of a Lipschitz function $\Sigma(t, x_s, u, \epsilon)$ mapping $[0,\infty) \times \mathfrak{X}_s(t) \times \mathbb{R}^l \times (0, \epsilon^*]$ into $\mathfrak{X}_f(t)$ and for every solution $x_s(t)$, $x_f(t)$ of Eq. 22 with $x_f(0) = \Sigma(0, x_s(0), u, \epsilon)$, then

$$x_f(t) = \Sigma(t, x_s(t), u, \epsilon), \forall t \geq 0 \qquad (24)$$

(iii) $\mathfrak{M}(t)$ attracts every trajectory exponentially.

On $\mathfrak{M}(t)$, the evolution of the state x_s is governed by the following finite-dimensional system

$$\frac{dx_s}{dt} = \mathcal{A}_s(t)x_s + \mathcal{B}_s(t)u + f_s[t, x_s, \Sigma(t, x_s, u, \epsilon)]$$
$$y_c = \mathcal{C}(t)[x_s + \Sigma(t, x_s, u, \epsilon)], y_m = \mathcal{S}(t)[x_s + \Sigma(t, x_s, u, \epsilon)] \quad (25)$$

where $\Sigma(t, x_s, u, \epsilon)$ is the solution of the following infinite-order partial differential equation

$$\epsilon\frac{\partial \Sigma}{\partial t} + \epsilon\frac{\partial \Sigma}{\partial x_s}[\mathcal{A}_s(t)x_s + \mathcal{B}_s(t)u + f_s(t, x_s, \Sigma)] + \epsilon\frac{\partial \Sigma}{\partial u}\dot{u}$$
$$= \mathcal{A}_{f\epsilon}(t)\Sigma + \epsilon\mathcal{B}_f(t)u + \epsilon f_f(t, x_s, \Sigma) \quad (26)$$

which $\Sigma(t, x_s, u, \epsilon)$ has to satisfy for all $t \in [0, \infty), x_s \in \mathcal{K}_s(t)$, $u \in \mathbb{R}^l$, $\epsilon \in (0, \epsilon^*]$. The complexity of Eqs. 26 does not allow computing a closed form solution for $\Sigma(t, x_s, u, \epsilon)$ in most practical applications including the crystal growth process. Therefore, the following approximation procedure, motivated by the two-time-scale property of the system of Eq. 22, is employed to compute approximations of $\Sigma(t, x_s, u, \epsilon)$ (approximate inertial manifolds). In particular, the vectors $\Sigma(t, x_s, u, \epsilon)$ and u are assumed to be given in a power series in ϵ

$$u = \bar{u}_0 + \epsilon\bar{u}_1 + \epsilon^2\bar{u}_2 + \ldots + \epsilon^k\bar{u}_k + O(\epsilon^{k+1})$$
$$\Sigma(t, x_s, u, \epsilon) = \Sigma_0(t, x_s, u) + \epsilon\Sigma_1(t, x_s, u) + \epsilon^2\Sigma_2(t, x_s, u)$$
$$+ \ldots + \epsilon^k\Sigma_k(t, x_s, u) + O(\epsilon^{k+1}) \quad (27)$$

where $\bar{u}_k$, Σ_k are smooth vector functions. Σ_k can be computed by substituting the expressions of Eq. 27 into Eq. 26, and equating terms of the same power in ϵ. For example, when $k = 0$, the expansion of Eq. 27 yields $\Sigma(t, x_s, u, \epsilon) = \Sigma_0(t, x_s, u) = 0$, and the corresponding approximation of the system of Eq. 25 is

$$\frac{dx_s}{dt} = \mathcal{A}_s(t)x_s + \mathcal{B}_s(t)\bar{u}_0 + f_s(t, x_s, 0)$$
$$y_c = \mathcal{C}(t)x_s, y_m = \mathcal{S}(t)x_s \quad (28)$$

which is identical to the one obtained from a direct application of Galerkin's method to the system of Eq. 22. On the other hand, for $k = 1$, the expansion of Eq. 27 yields $\Sigma(t, x_s, u, \epsilon) = \epsilon\Sigma_1(t, x_s, \bar{u}_0) = -\epsilon(\mathcal{A}_{f\epsilon})^{-1}(t)[\mathcal{B}_f(t)\bar{u}_0 + f_f(t, x_s, 0)]$ (note that from assumption 4 we have that $(\mathcal{A}_{f\epsilon})^{-1}(t)$ exists and is bounded, $\forall t > 0$), and the corresponding approximation of the system of Eq. 25 is

$$\frac{dx_s}{dt} = \mathcal{A}_s(t)x_s + \mathcal{B}_s(t)(\bar{u}_0 + \epsilon\bar{u}_1) + f_s(t, x_s, \epsilon\Sigma_1(t, x_s, \bar{u}_0))$$
$$y_c = \mathcal{C}(t)[x_s + \epsilon\Sigma_1(t, x_s, \bar{u}_0)]$$
$$y_m = \mathcal{S}(t)[x_s + \epsilon\Sigma_1(t, x_s, \bar{u}_0)] \quad (29)$$

Even though the system of Eq. 29 has the same dimension with the one of Eq. 28, it is a more accurate approximation of the infinite-dimensional system of Eq. 20; the reader may refer to Armaou and Christofides (1999) for a precise characterization of the accuracy of both systems. Therefore, the system of Eq. 29 will be used for the synthesis of an output feedback controller in the next subsection.

Nonlinear output feedback control

In this section, we synthesize nonlinear finite-dimensional output feedback controllers that guarantee local exponential stability and force the controlled output of the closed-loop PDE system to follow a prespecified response, provided that ϵ is sufficiently small. The output feedback controllers are constructed on the basis of the system of Eq. 29 through a combination of state feedback controllers with state observers.

More specifically, we use the system of Eq. 29 to synthesize nonlinear state feedback controllers of the following general form

$$u = \bar{u}_0 + \epsilon\bar{u}_1 = p_0(t, x_s) + Q_0(t, x_s)v + \epsilon[p_1(t, x_s) + Q_1(t, x_s)v] \quad (30)$$

where $p_0(t, x_s)$, $p_1(t, x_s)$ are smooth vector functions, $Q_0(t, x_s)$, $Q_1(t, x_s)$ are smooth matrices, and $v \in \mathbb{R}^l$ is the constant reference input vector. The nonlinear controllers are constructed by following a sequential procedure. Specifically, the component $\bar{u}_0 = p_0(t, x_s) + Q_0(t, x_s)v$ is initially synthesized on the basis of the system of Eq. 28, and then the component $\bar{u}_1 = p_1(t, x_s) + Q_1(t, x_s)v$ is synthesized on the basis of the system of Eq. 29. The synthesis of $[p_\nu(t, x_s), Q_\nu(t, x_s)]$, $\nu = 0, 1$, so that a nonlinear controller of the form of Eq. 30 guarantees local exponential stability and forces the output of the system of Eq. 29 to follow a desired linear response, is performed by utilizing geometric control methods for nonlinear ODEs (the details of the controller synthesis can be found in Isidori (1989) and are omitted for brevity).

Since measurements of $\bar{x}(z, t)$ (and thus, $x_s(t)$) are usually not available in practice, we assume that there exists an L so that the nonlinear dynamical system

$$\frac{d\eta}{dt} = \mathcal{A}_s(t)\eta + \mathcal{B}_s(t)[\bar{u}_0 + \epsilon\bar{u}_1] + f_s[t, \eta, \epsilon\Sigma_1(t, \eta, u)]$$
$$+ L\{y_m - \mathcal{S}(t)[\eta + \epsilon\Sigma_1(t, \eta, u)]\} \quad (31)$$

where η denotes and m-dimensional state vector, is a local exponential observer for the system of Eq. 29 (that is, the discrepancy $|\eta(t) - x_s(t)|$ tends exponentially to zero).

Theorem 1 that follows provides the synthesis formula of the output feedback controller and conditions that guarantee closed-loop stability. To state our result, we need to use the Lie derivative notation and the concepts of relative order and characteristic matrix (which are defined in the appendix), for the system of Eq. 29. The proof of the theorem is given in Armaou and Christofides (1999).

Theorem 1: *Consider the parabolic PDE system of Eq. 20 and assume that the fast subsystem of Eq. 23 is exponentially*

stable. Consider also the $O(\epsilon^2)$ approximation of the inertial form and assume that its characteristic matrix $C_1(t, x_s, \epsilon)$ is invertible $\forall t \in [0, \infty)$, $\forall x_s \in \mathcal{K}_s(t)$, $\forall \epsilon \in (0, \epsilon^*]$. Suppose also that the following conditions hold

(1) *The roots of the equation:*

$$\det(B(s)) = 0 \tag{32}$$

where $B(s)$ is an $l \times l$ matrix whose (i,j)-th element is of the form $\sum_{k=0}^{r_i} \beta_{jk}^i s^k$, lie in the open left-half of the complex plane, where β_{jk}^i are adjustable controller parameters.

(2) *The zero dynamics of the $O(\epsilon^2)$ approximation of the inertial form are locally exponentially stable.*

Then, there exist positive real numbers $\tilde{\mu}_1$, $\tilde{\mu}_2$, $\tilde{\epsilon}^*$ such that if $|x_s(0)| \le \tilde{\mu}_1$, $\| x_f(0) \|_2 \le \tilde{\mu}_2$ and $\epsilon \in (0, \tilde{\epsilon}^*]$, and $\eta(0) = x_s(0)$, the dynamic output feedback controller

$$\begin{aligned}
\frac{d\eta}{dt} &= \mathcal{A}_s(t)\eta + \mathcal{B}_s(t)[\bar{u}_0(t,\eta) + \epsilon \bar{u}_1(t,\eta)] \\
&\quad + f_s\Big\{t, \eta, \epsilon(\mathcal{A}_{f\epsilon})^{-1}(t)[-\mathcal{B}_f(t)\bar{u}_0(t,\eta) - f_f(t,\eta,0)]\Big\} \\
&\quad + L\Big[y_m - \Big\{\mathcal{S}(t)\eta + \mathcal{S}(t)\epsilon(\mathcal{A}_{f\epsilon})^{-1}(t)[-\mathcal{B}_f(t)\bar{u}_0(t,\eta) \\
&\qquad - f_f(t,\eta,0)]\Big\}\Big] \\
u = \bar{u}_0(t,\eta) + \epsilon \bar{u}_1(t,\eta) &:= \Big\{[\beta_{1r_1} \cdots \beta_{lr_l}] C_0(t,\eta)\Big\}^{-1} \\
&\quad \times \Big\{\upsilon - \sum_{i=1}^{l} \sum_{k=0}^{r_i} \beta_{ik} L_{f_0}^k h_{0_i}(t,\eta)\Big\} \\
&\quad + \epsilon\Big\{[\beta_{1r_1} \cdots \beta_{lr_l}] C_1(t,\eta,\epsilon)\Big\}^{-1} \\
&\quad \times \Big\{\upsilon - \sum_{i=1}^{l} \sum_{k=0}^{r_i} \beta_{ik} L_{f_1}^k h_{1i}(t,\eta,\epsilon)\Big\}
\end{aligned} \tag{33}$$

(a) *Guarantees local exponential stability of the closed-loop system, and*

(b) *ensures that the outputs of the closed-loop system satisfy for all $t \in [t_b, \infty)$*

$$y_{c_i}(t) = y_{cs_i}(t) + O(\epsilon^2), \; i = 1, \ldots, l \tag{34}$$

where t_b is the time required for the off-manifold fast transients to decay to zero exponentially, and $y_{cs_i}(t)$ is the solution of

$$\sum_{i=1}^{l} \sum_{k=0}^{r_i} \beta_{ik} \frac{d^k y_{cs_i}}{dt^k} = \upsilon \tag{35}$$

Remark 3: The implementation of the controller of Eq. 33 requires to explicitly compute the vector function $\Sigma_1(t, \eta, \bar{u}_0)$. However, $\Sigma_1(t, \eta, \bar{u}_0)$ has an infinite-dimensional range and therefore cannot be implemented in practice. Instead, a finite-dimensional approximation of $\Sigma_1(t, \eta, \bar{u}_0)$, say $\Sigma_{1t}(t, \eta, \bar{u}_0)$, can be derived by keeping the first $\tilde{m}$ elements of $\Sigma_1(t, \eta, \bar{u}_0)$ and neglecting the remaining infinite ones. Clearly, as $\tilde{m} \to \infty$, $\Sigma_{1t}(t, \eta, \bar{u}_0)$ approaches $\Sigma_1(t, \eta, \bar{u}_0)$. This implies that by picking $\tilde{m}$ to be sufficiently large, the controller of Eq. 33 with $\Sigma_{1t}(t, \eta, \bar{u}_0)$ instead of $\Sigma_1(t, \eta, \bar{u}_0)$ guarantees stability and enforces the requirement of Eq. 35 in the closed-loop infinite-dimensional system.

Remark 4: Note that in the presence of small initialization errors of the observer states (that is, $\eta(0) \neq x_s(0)$), uncertainty in the model parameters and external disturbances, although a slight deterioration of the performance may occur, (that is, the requirement of Eq. 34 will not be exactly imposed in the closed-loop system), the output feedback controller of theorem 1 will continue to enforce exponential stability and asymptotic output tracking in the closed-loop system. Furthermore, the assumption that the characteristic matrix $C_1(t, x_s, \epsilon)$ is invertible $\forall t \in [0, \infty)$, $\forall x_s \in \mathcal{K}_s(t)$, $\forall \epsilon \in (0, \epsilon^*]$ is made in order to simplify the development and can be relaxed by using dynamic state feedback instead of static state feedback (see Isidori (1989) for details). Finally, it can be shown using singular perturbations that the nonlinear controller of Eq. 33 possesses a robustness property with respect to fast and asymptotically stable unmodeled dynamics (that is, actuator and sensor dynamics, fast process dynamics, and so on). A comprehensive study of the robustness of the nonlinear controller of Eq. 33 in the presence of various sources of uncertainty for the crystal growth process is presented later.

Remark 5: Finally, we note that the nonlinear model reduction and control methods of this and the previous subsection can be readily generalized to parabolic PDE systems in which the manipulated inputs enter in a nonlinear fashion and can be represented by the following infinite-dimensional form

$$\begin{aligned}
\dot{x} &= \mathcal{A}(t)x + \mathcal{B}(t)g(u) + f(t,x), \quad x(0) = x_0 \\
y_c &= \mathcal{C}(t)x, \; y_m = \mathcal{S}(t)x
\end{aligned} \tag{36}$$

where $g(\cdot)$ is a nonlinear smooth function. This can be done by using $g(u)$ as a "virtual manipulated input," computing a virtual control action u_v for $g(u)$, and then solving through Newton's method the nonlinear equation $g_u = u_v$ at each time instant to compute the value of u (the reader may refer to the next section for an application of this approach to the Czochralski crystal growth process where the manipulated input T_κ (κ-th heater temperature) enters the PDE in the form T_i^4 due to the nonlinear dependence of the radiation mechanism on temperature).

Crystal Temperature Regulation in the Czochralski Growth

Nonlinear model reduction

In this section, our objective is to synthesize and implement a low-order nonlinear output feedback controller on the crystal growth process that enforces a desired smooth temperature profile in the axial direction inside the crystal. We begin with the reduction of the 1-D parabolic PDE model of Eq. 12–13 into a small set of nonlinear ODEs utilizing the model reduction algorithm discussed earlier. This set of ODEs will be subsequently used for controller design.

The 1-D model of Eqs. 12–13 can be formulated in the general form of Eqs. 14–16 with

$$A = 0.0,\ B = \frac{k}{\rho c_p},\ w = \frac{\sigma \epsilon_{w_{cr}}}{\rho c_p},$$

$$b(z,t) = \left[\epsilon_{w_1} \left(\frac{2}{R} F_{cr\to 1}(R,z) + \frac{\delta(z-l(t))}{kl(t)} F_{cr\to 1}(z) \right) T_{1_{set}}^4 \right.$$
$$\left. \cdots \epsilon_{w_m} \left(\frac{2}{R} F_{cr\to 3}(R,z) + \frac{\delta(z-l(t))}{kl(t)} F_{cr\to 3}(z) \right) T_{3_{set}}^4 \right],$$

$$f(z,t,T_c) = -v_p \frac{\partial T_c}{\partial z} + \frac{2\sigma \epsilon_{w_{cr}}}{\rho c_p R} \left(\epsilon_{w_m} F_{cr\to m}(R,z)\left[T_m^4 - T_c^4\right] \right.$$
$$\left. + \epsilon_{w_{ch}} F_{cr\to ch}(R,z)\left[T_{ch}^4 - T c^4\right] - \sum_{i=1}^{n} \epsilon_{w_i} F_{cr\to i}(R,z) T_c^4 \right)$$
$$+ \delta(z-l(t)) \frac{\sigma \epsilon_{w_{cr}}}{k\rho c_p l(t)} \left(\epsilon_{w_m} F_{cr\to m}(z)\left[T_m^4 - T_c^4\right] \right.$$
$$\left. + \epsilon_{w_{ch}} F_{cr\to ch}(z)\left[T_{ch}^4 - T_c^4\right] - \sum_{i=1}^{3} \epsilon_{w_i} F_{cr\to i}(z) T_c^4 \right) \quad (37)$$

where $\delta(\cdot)$ is the standard Dirac function. Defining the new variable $x = (T_c - T_{mp})/(T_{mp})$ and nondimensionalizing the temperature for this parabolic PDE system, the spatial differential operator $\mathfrak{A}$ can be defined as

$$\mathfrak{A}(t)x = \frac{k}{\rho c_p} \frac{\partial^2 \bar{x}}{\partial z^2}, \quad x \in D[\mathfrak{A}(t)]$$
$$= \left\{ x \in \mathfrak{K}([0, l(t)]; \mathbb{R});\ \bar{x}(0,t) = 0;\ \frac{\partial \bar{x}}{\partial z}[l(t), t] = 0 \right\} \quad (38)$$

Note that $\mathfrak{A}(t)$ includes the higher-order spatial derivative (conduction term) included in the PDE of Eq. 12, while owing to the time-dependent nature of the pulling rate v_p (in general) it does not include the first-order spatial derivative (convective term). The eigenvalue problem of $\mathfrak{A}$ can be solved analytically and yields

$$\lambda_j(t) = -\frac{k}{\rho c_p} \left[\frac{\pi(2j+1)}{2l(t)} \right]^2,$$
$$\phi_j(t,z) = \sqrt{\frac{2}{l(t)}} \sin\left(\frac{\pi(2j+1)}{2l(t)} z \right), \quad j = 0, \ldots, \infty \quad (39)$$

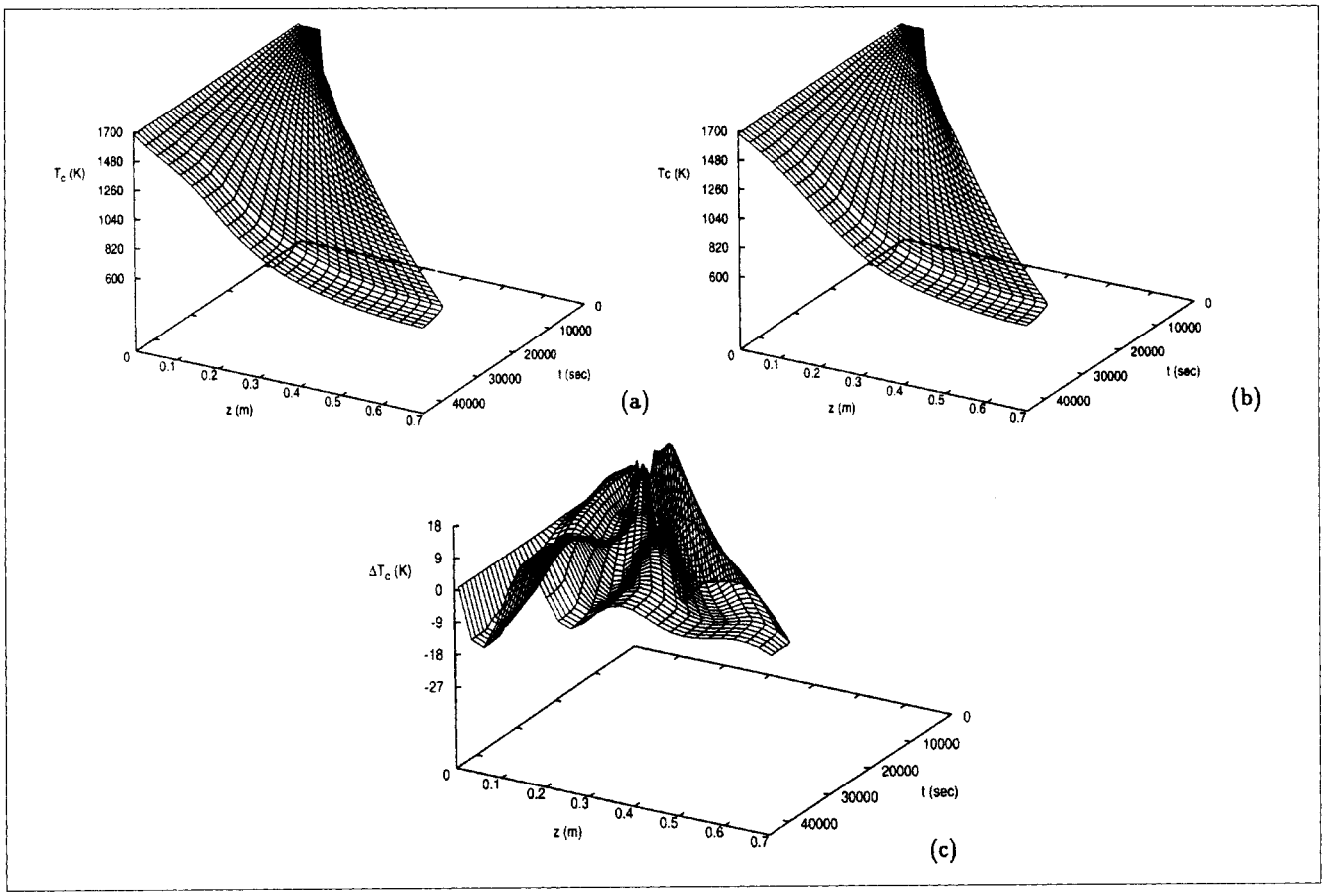

Figure 12. Comparison of temperature profiles of open loop system at T_{amb} = 600 K.

(a) 2-D model at $r = 0.034$ m; (b) reduced-order model (c) temperature difference between the 2-D model at $r = 0.034$ m and the reduced-order model.

Table 4. Control Parameters

Controller κ	$z_{s\kappa}$ [m]	z_{f_κ} [m]	$z_{m\kappa}$ [m]	β_κ	T_s [K]
1	0.18	0.38	0.28	1.0	1,400
2	0.38	0.58	0.48	1.0	1,250
3	0.58	0.71	0.68	1.0	1,100

where the eigenfunctions $\phi_j(t,z)$ form a countable, $\forall t \in [0,\infty)$, and orthogonal basis of $\mathfrak{R}(t)$.

We used the nonlinear model reduction method discussed earlier, that is, combination of Galerkin's method with approximate inertial manifolds, to derive a fourth-order ODE model which uses a 4-th order approximation for x_f (that is, $m=4$ and $\tilde{m}=4$). The eigenfunctions $\phi_j(t,z)$ were used as basis functions in Galerkin's method. Figure 12 shows the temporal evolution of the crystal temperature in the axial direction at $r=0.034$ computed by the 2-D model (Figure 12a), the temporal evolution of the crystal temperature in the axial direction computed by the fourth-order model (Figure 12b), and the difference between the crystal temperatures predicted by the 2-D model ($r=0.034$) and the fourth-order model (Figure 12c), for $T_{\text{amp}}=600$. It is clear that the predictive capabilities of the reduced-order model are very good for a wide range of operating conditions, and, thus, it makes sense to use this fourth-order model as a basis for the synthesis of a nonlinear output feedback controller.

Nonlinear controller synthesis: closed-loop simulations

The control objective is to enforce an almost linear axial temperature profile in the crystal by manipulating the temperature of the heaters and using point measurements of the surface temperature of the crystal. Specifically, we consider the control configuration shown in Figure 11. The heater was assumed to be divided into three equispaced regions and the temperature in each one of these regions is adjusted by the controller. The region where the i-th controller operates is determined by the variables z_{si}, z_{fi}, which represent the minimum and maximum distances of the controller region from the melt-crystal interface, respectively, (note that the distribution function of the i-th control actuator is $b_i(z)=H(z-z_{si})-H(z-z_{fi})$ where $H(\cdot)$ is the standard Heavyside function). The controlled and measured outputs were taken to be identical and defined as

$$y_{c1}(t)=y_{m1}(t)=\int_0^{l(t)}\delta(z-z_{m1})T_c(R,z,t)dz$$

$$y_{c2}(t)=y_{m2}(t)=\int_0^{l(t)}\delta(z-z_{m2})T_c(R,z,t)dz$$

$$y_{c3}(t)=y_{m3}(t)=\int_0^{l(t)}\delta(z-z_{m3})T_c(R,z,t)dz \quad (40)$$

where $T_c(R,z,t)$ is the surface temperature of the crystal. The point measurements of the temperature on the surface of the crystal can be readily obtained in practice with optical pyrometers. Finally, the fourth-order model obtained through Galerkin's method with approximate inertial manifolds with the specifications for manipulated inputs, controlled and measured outputs was used for the synthesis of a nonlinear output feedback controller by utilizing the formula of theorem 1. In order to incorporate integral action in this controller, the term $v_i - h_{0i}(\eta)$ was substituted by the term $v_i - y_{ci}$. All the parameters used in the control problem are given in Table 4.

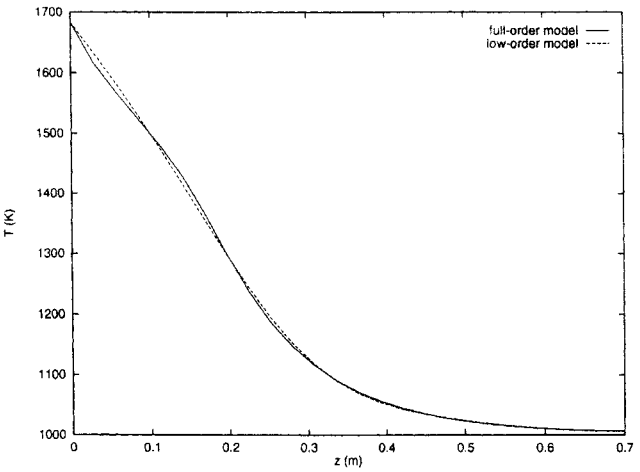

Figure 13. Comparison of temperature profiles of open loop system at $T_{\text{amb}}=600$ K between the 2-D model at $r=0.05$ m and the reduced-order model at the end of the process.

Several simulations runs were performed to evaluate; (a) the ability of the nonlinear controller to enforce a linear temperature profile in the axial direction inside the crystal; (b) the robustness properties of the nonlinear controller with respect to parametric model uncertainty, disturbances and unmodeled actuator and sensor dynamics. In all the simulation runs, the crystal was initially ($t=0$ s) assumed to be at $T_c(z,r,0)=1{,}670$ K and have a length of $l(0)=0.05$ m. The initial conditions of the fourth-order observer included in the nonlinear output controller were computed by using the initial condition assumed for the crystal. Moreover, in all the simulation runs, the objective of the controller is to regulate the three controlled outputs at $y_{c1}=1{,}400$ K, $y_{c2}=1{,}250$ K, $y_{c3}=1{,}100$ K; this is motivated by our objective to enforce a linear temperature drop inside the crystal of 8 K/cm. As we will see in our results below, these set points allow enforcing a smooth linear temperature drop inside the crystal at all times during the growth. Furthermore, we note that in order to avoid disturbing the concentration profiles of the dopant and oxygen through unnecessarily large variations of the manipulated inputs, a lower bound (constraint) is implemented on the control action which does not allow $u_i(t)$ to become smaller than 0.82 (note that $u_i(t)=T_i/T_{sp_i}$ where $T_{sp_i}=1{,}000$ K for all $i=1, 2, 3$ is a reference temperature for the i-th heater). Finally, the tuning parameters of the nonlinear controller are chosen so that the computed variations in the control action with respect to time are small.

Initially, the set point tracking capability of the nonlinear controller was evaluated under nominal conditions. Figures 14 and 15a show the contour plots of the crystal temperature as a function of the axial and radial directions at four different time instants during the operation of the process and the temporal evolution of the crystal temperature in the axial di-

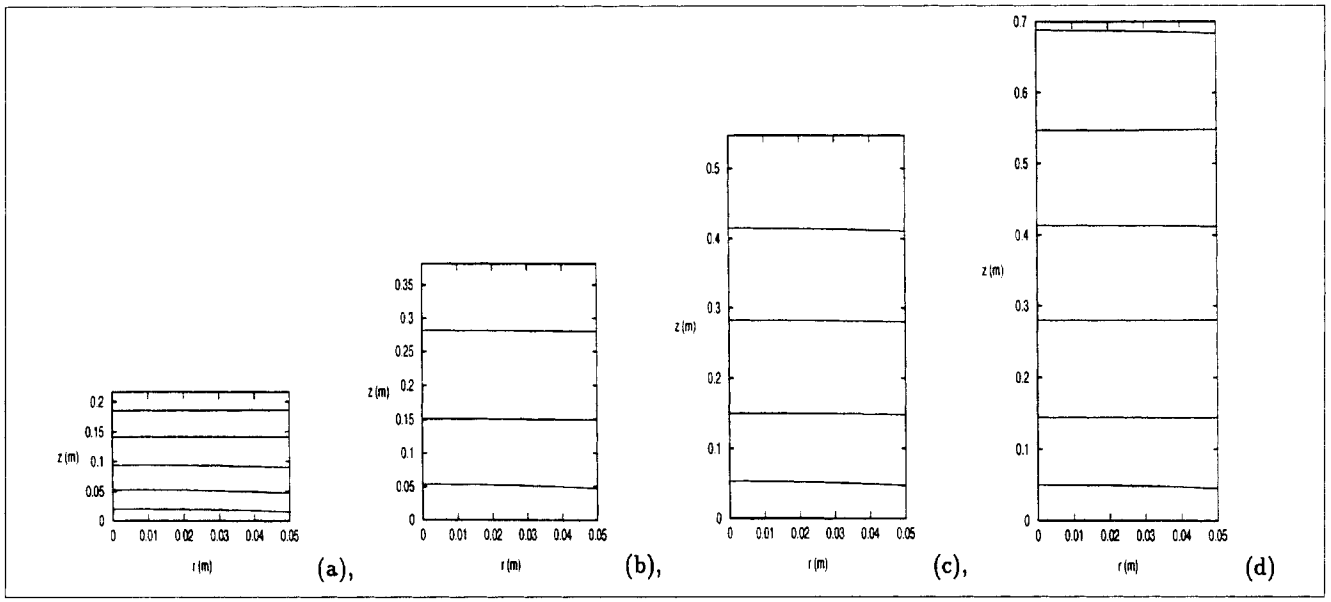

Figure 14. Temperature of crystal as a function of radial and axial coordinates under nonlinear control-nominal case.
(a) $t = 1 \times 10^4$ s; (b) $t = 2 \times 10^4$ s; (c) $t = 3 \times 10^4$ s and (d) $t = 4 \times 10^4$ s. Each contour represents a 100 K temperature difference.

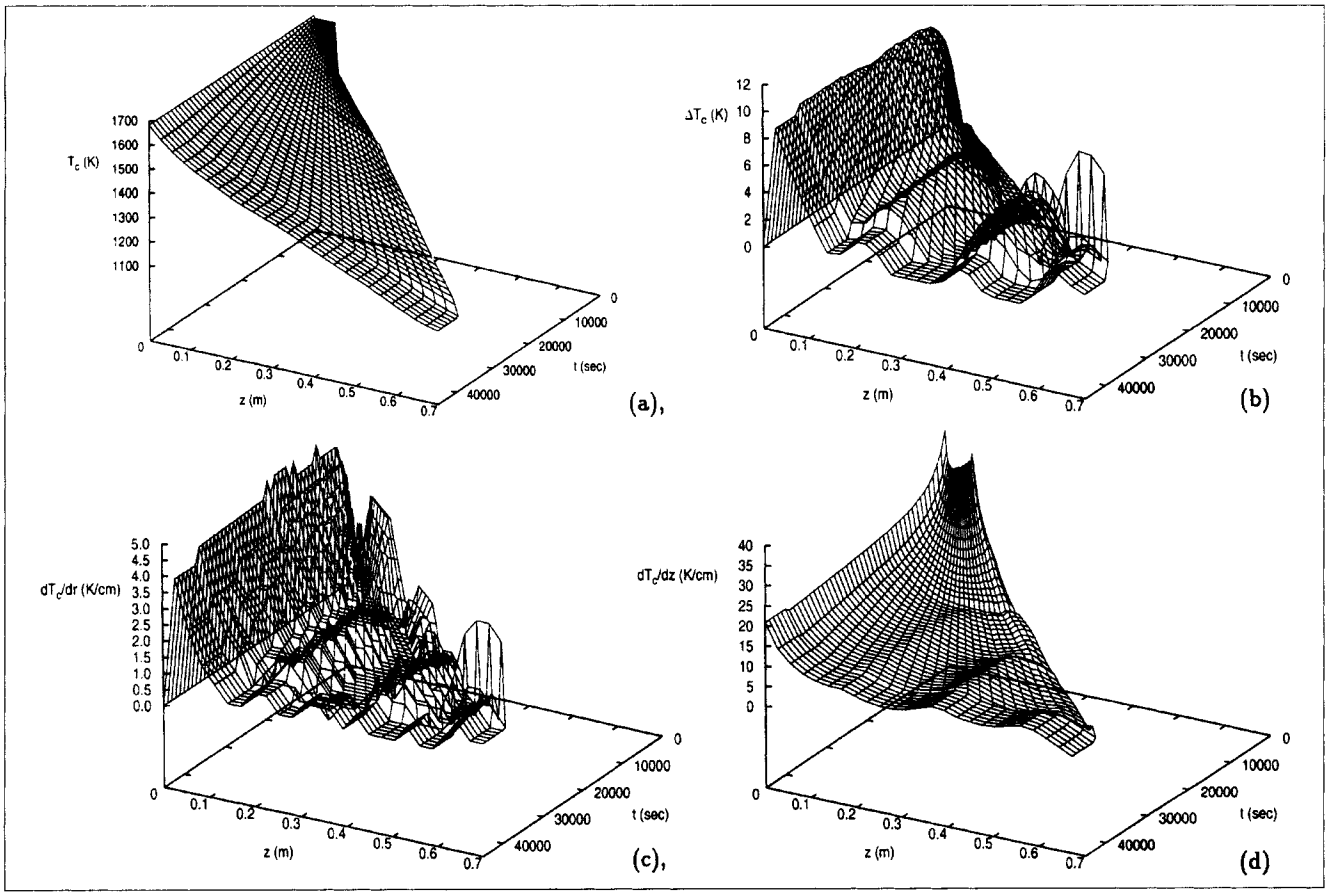

Figure 15. (a) Temperature of crystal at $r = 0.0$ m; (b) maximum temperature difference inside the crystal in the radial direction; (c) maximum thermal gradient inside the crystal in the radial direction; (d) maximum thermal gradient inside the crystal in the axial direction, as a function of time and axial coordinate under nonlinear control-nominal case.

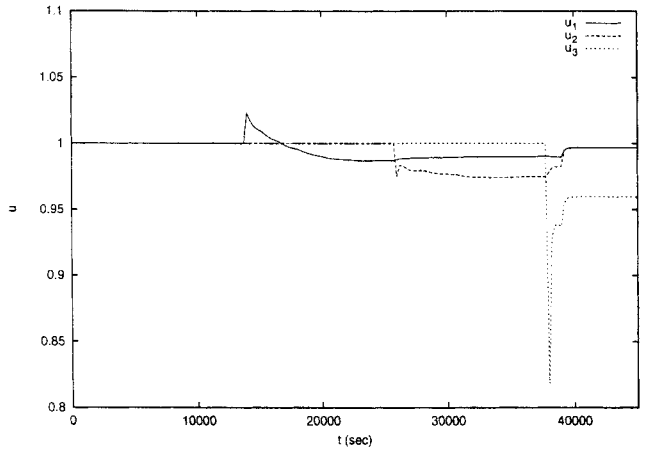

Figure 16. Manipulated input profiles-nominal case.

rection at the center of the crystal, respectively, in the closed-loop system. Clearly, the nonlinear controller drives the controlled outputs to their new set points, while enforcing the desired temperature drop inside the crystal at all radial positions (note that the radial temperature nonuniformity is less than 20 K which is clearly smaller to the one computed for the open-loop system; compare Figure 15b and Figure 3b), without creating large radial temperature gradients at any time (the radial temperature gradients remain small for all times; see Figure 15c and compare with 3c). As can be seen from Figure 15d, the temperature gradient in the axial direction remains bounded throughout the length of the crystal, and is much smaller than in the open loop case (Figure 3d). Figure 16 show the corresponding profiles for the three manipulated inputs, which change smoothly with time to achieve the control objective. Note also that each one of the three controllers is activated [that is, $u_i(t) \neq 1$] when the crystal enters in the zone in which the corresponding control actuator operates and the initial sharp profiles are actually the slow activation of the controllers over a period of 250 s. Figure 17a shows the crystal temperature at $r = 0.05$ m, and Figure 17b shows the maximum thermal gradient inside the crystal in the axial direction, at the end of the process cycle under the proposed nonlinear control system, the PI controller, and the case of constant ambient temperature; it is clear that the proposed control scheme reduces the thermal gradients in the axial direction compared to the other approaches.

Next, the robustness properties of the nonlinear controller in the presence of parametric uncertainties, disturbances, and unmodeled actuator and sensor dynamics were investigated. Figures 18 and 19a show the crystal temperature contours as a function of the axial and radial directions at four different time instants during the operation of the process and the temporal evoluton of the closed-loop crystal temperature in the axial direction at the center of the crystal, respectively, in the presence of 10% error in the emissivity of the crystal $e_{w_{cr}}$. The nonlinear controller exhibits very good robustness properties, driving the output to its set point with small temperature gradients in the radial (Figure 19c) and axial (Figure 19d) directions (compare with the open-loop temperature gradient profiles Figures 19c and 19d) while requesting smooth control actions (Figure 20). Figure 23 shows the crystal temperature contours at four different time instants and Figure 24a shows the closed-loop crystal temperature in the axial direction at the center of the crystal in the presence of a 10% disturbance in the melt temperature and 20% disturbance in the temperature of the chamber, while Figure 25 shows the manipulated input profiles. Again, the nonlinear controller enforces the desired linear drop in the crystal temperature in the axial direction, attenuating the effect of the disturbances (compare the closed-loop temperature profiles of Figure 24 with the open-loop temperature profiles of Figure 21 and 22 ($T_{amb} = 1{,}000$ K), under the same disturbances), while keeping the temperature gradients in the radial (Figure 19c) and axial (Figure 19d) directions small.

Figures 26 and 27a show the closed-loop crystal temperature as a function of the axial and radial directions at four different time instants during the operation of the process and the temporal evolution of the closed-loop crystal temperature in the axial direction at the center of the crystal, respectively, in the presence of the unmodeled actuator and sensor dynamics, and Figure 28 shows the manipulated input profiles. To account for the actuator dynamics, the process model of Eq. 1 was augmented with the dynamical system $\epsilon_c \dot{z}_{1i} = -z_{1i} + z_{2i}$, $\epsilon_c \dot{z}_{2i} = -z_{2i} + u_i$, $i = 1, 2, 3$, where z_{1i},

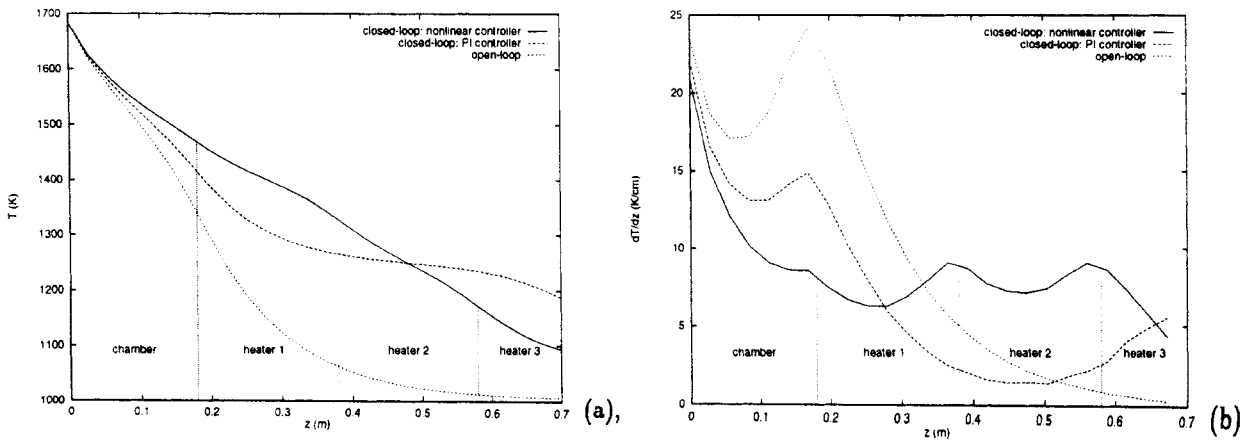

Figure 17. (a) Temperature of crystal at $r = 0.05$ m; (b) maximum thermal gradient inside the crystal in the axial direction, at the end of the process-nominal case.

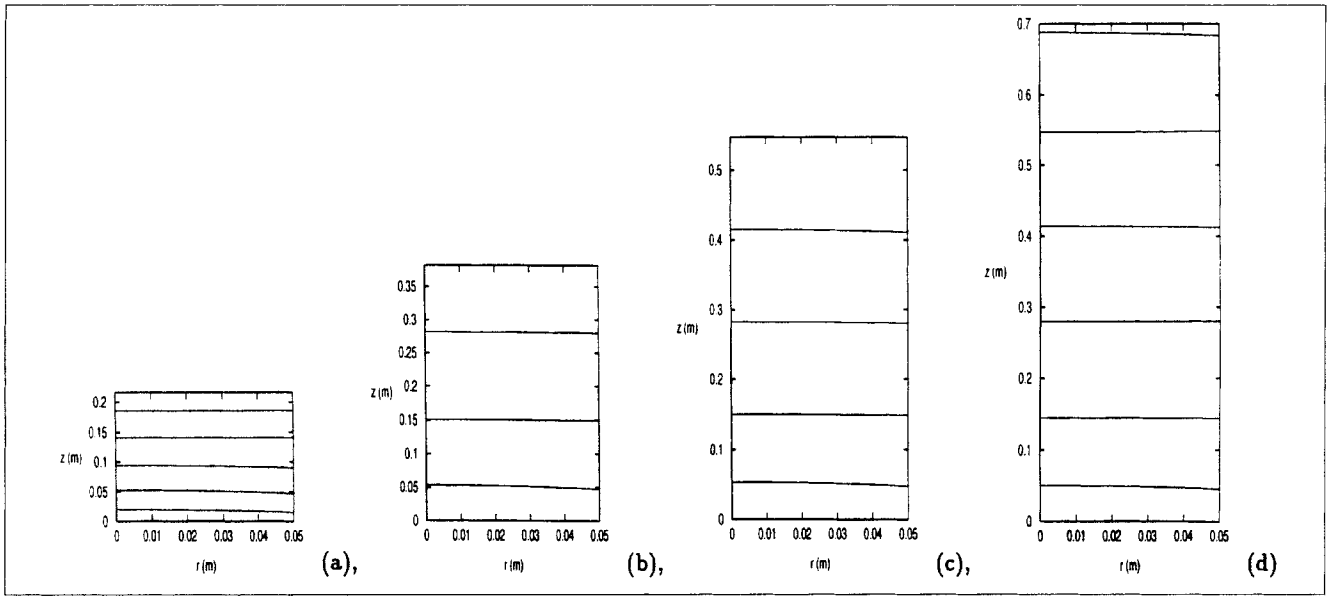

Figure 18. Temperature of crystal as a function of radial and axial coordinates under nonlinear control-parametric uncertainty.

(a) $t = 1 \times 10^4$ s, (b) $t = 2 \times 10^4$ s, (c) $t = 3 \times 10^4$ s and (d) $t = 4 \times 10^4$ s. Each contour represents a 100 K temperature difference.

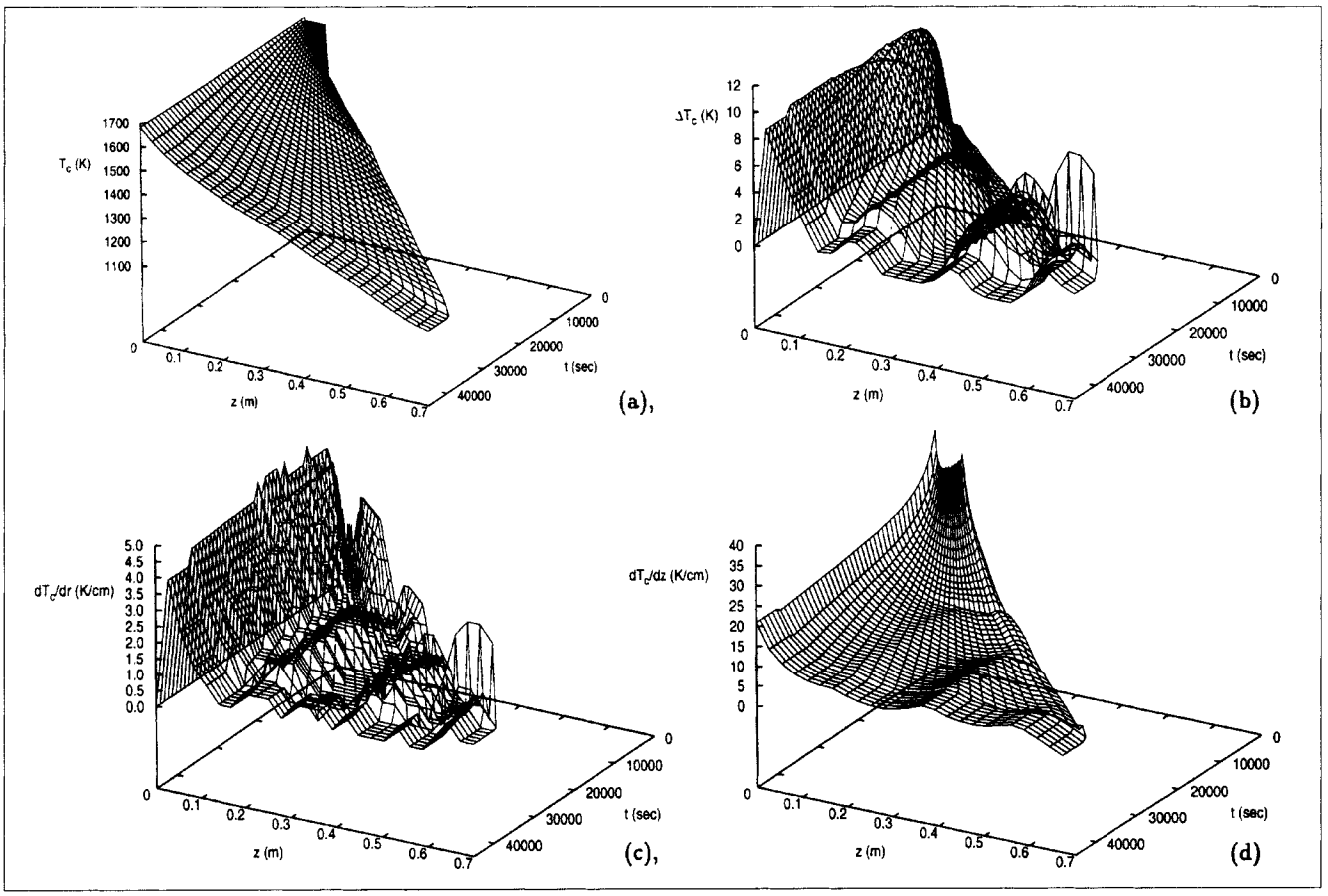

Figure 19. (a) Temperature of crystal at $r = 0.0$ m; (b) maximum temperature difference inside the crystal in the radial direction; (c) maximum thermal gradient inside the crystal in the radial direction; (d) maximum thermal gradient inside the crystal in the axial direction, as a function of time and axial coordinate under nonlinear control-parametric uncertainty.

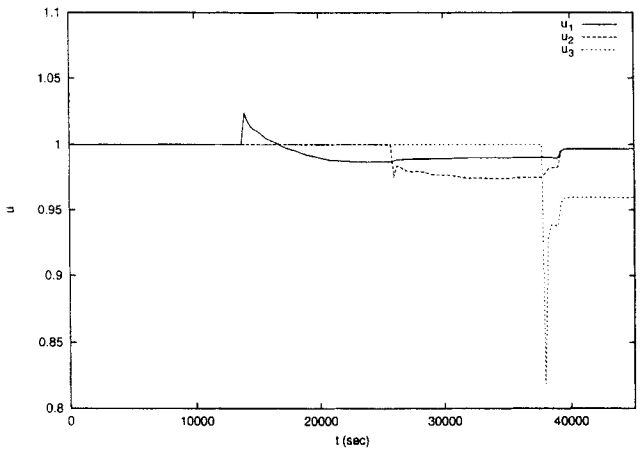

Figure 20. Manipulated input profiles-parametric uncertainty.

$z_{2i} \in \mathbb{R}$ are the actuator states, z_{1i} is the actuator output, and ϵ_c is a small parameter characterizing how fast are the actuator dynamics. To account for the sensor dynamics, the process model of Eq. 1 was augmented with the dynamical system $\epsilon_m \dot{z}_{3i} = -z_{3i} + z_{4i}$, $\epsilon_m \dot{z}_{4i} = -z_{4i} + y_{mi}$, $i = 1, 2, 3$, where z_{3i}, $z_{4i} \in I\mathbb{R}$ are the sensor states, z_{3i} is the sensor output, and ϵ_m is a small parameter characterizing how fast are the sensor dynamics. We found that the maximum values of ϵ_c and ϵ_m for which the stability of the closed-loop system is guaranteed are $\epsilon_c = 0.02$ and $\epsilon_m = 0.02$, thereby implying that the nonlinear controller is robust with respect to stable and sufficiently fast unmodeled sensor and actuators dynamics. From the results of the simulation study, it is evident that the nonlinear controller which was synthesized on the basis of a fourth-order model constructed through a combination of Galerkin's method and approximate inertial manifolds, possesses excellent closed-loop performance and robustness properties.

Finally, it is important to point out another advantage of the proposed control configuration. Even though there is no explicit way to reduce the thermal gradients in the radial direction inside the crystal through direct feedback control, reduction of such gradients is accomplished indirectly during the regulation of the thermal gradients in the axial direction, due to the well regulated environment in which the crystal grows in such a case. This point is made clear by comparing Figures 3c, 5c, 7c and 22c with Figures 15c, 19c, 24c and 27c that present the evolution of the radial thermal gradients inside the crystal in the open- and closed-loop systems, respectively, and show that a significant reduction of the thermal gradients in the radial direction is achieved in the case of using the proposed control scheme compared to the open-loop system.

Remark 6: The decision to pick the three set point values so that an almost linear axial temperature drop is enforced inside the crystal was motivated by our objective to reduce the axial thermal gradient $\partial T_c/\partial z$ for all $z \in [0, l(t)]$ and all $t \in [0, \infty)$, thereby reducing the possibilities for crystal dislocation and defects due to temperature nonuniformity (refer to Gevelber (1994a) and Szabó (1985) for more information). We note that the nonlinear controller can be used to enforce other desired smooth temperature drops inside the crystal by appropriate choice of the values of the three set points.

Remark 7: It is important to point out that even though the fourth-order model obtained through Galerkin's method and approximate inertial manifolds was used to synthesize a nonlinear geometric controller which can be readily implemented in practice, this fourth-order model can also be used for the design of optimization-based controllers including

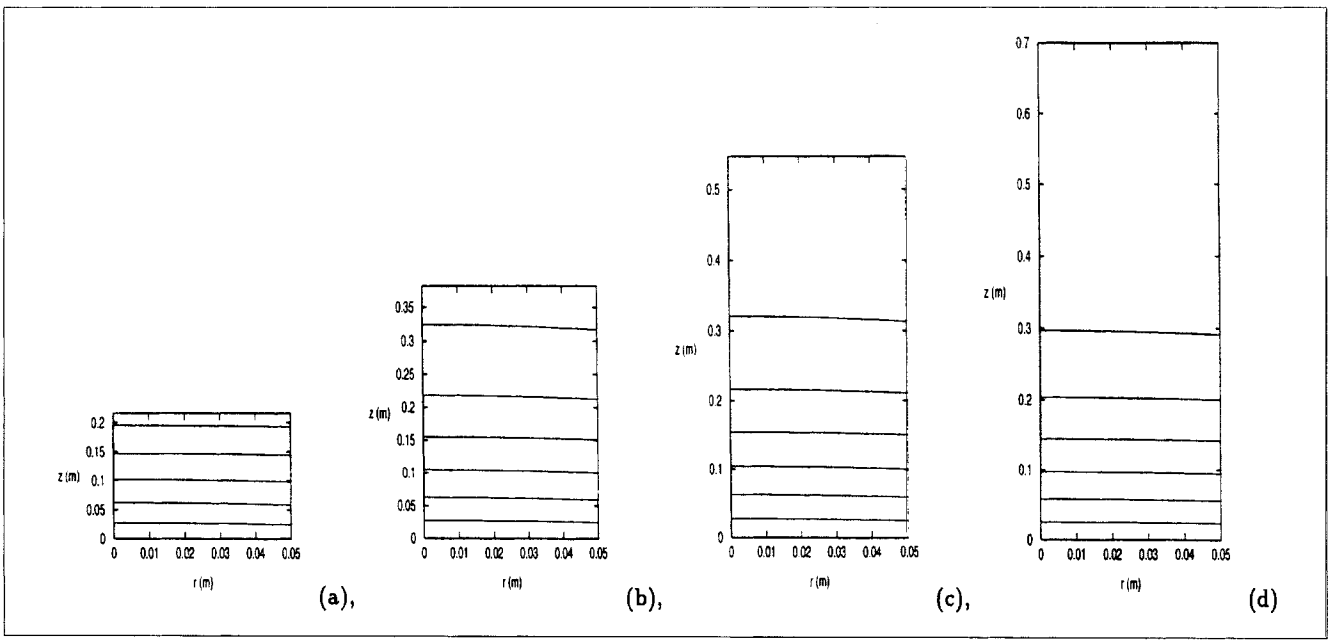

Figure 21. Temperature of crystal as a function of radial and axial coordinates for T_{amb} = 1,000 K-exogenous disturbances.

(a) $t = 1 \times 10^4$ s; (b) $t = 2 \times 10^4$ s; (c) $t = 3 \times 10^4$ s, (d) $t = 4 \times 10^4$ s. Each contour represents a 100 K temperature difference.

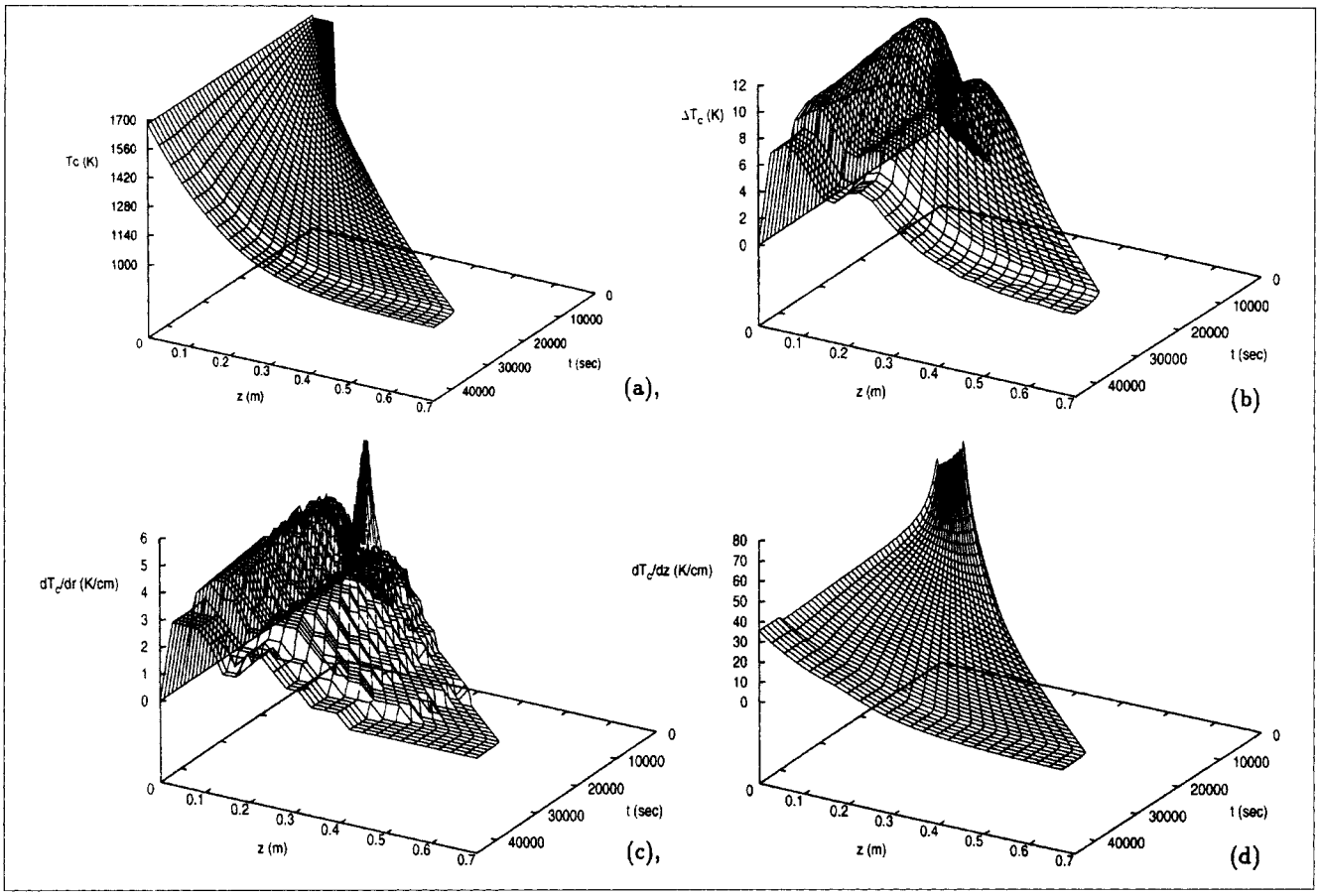

Figure 22. (a) Temperature of crystal at $r = 0.0$ m; (b) maximum temperature difference inside the crystal in the radial direction; (c) maximum thermal gradient inside the crystal in the radial direction; (d) maximum thermal gradient inside the crystal in the axial directions as a function of time and axial coordinate for $T_{amb} = 1{,}000$ K-exogenous disturbances.

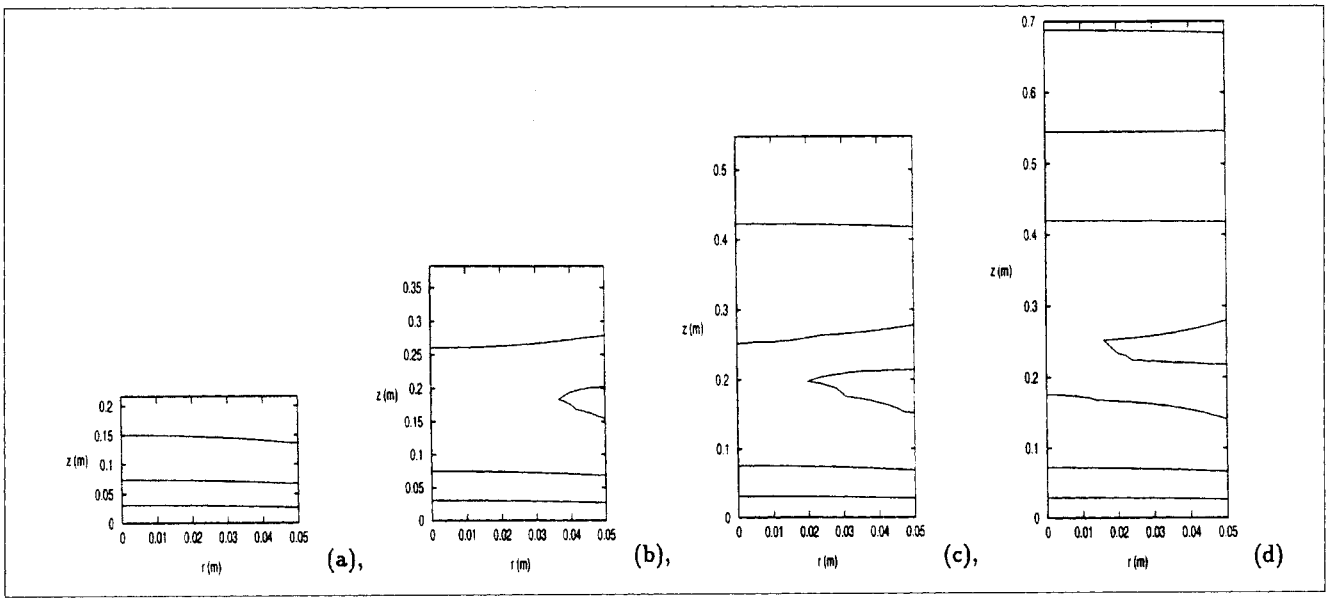

Figure 23. Temperature of crystal as a function of radial and axial coordinates under nonlinear control-exogenous disturbances.

(a) $t = 1 \times 10^4$ s; (b) $t = 2 \times 10^4$ s; (c) $t = 3 \times 10^4$ s; (d) $t = 4 \times 10^4$ s. Each contour represents a 100 K temperature difference.

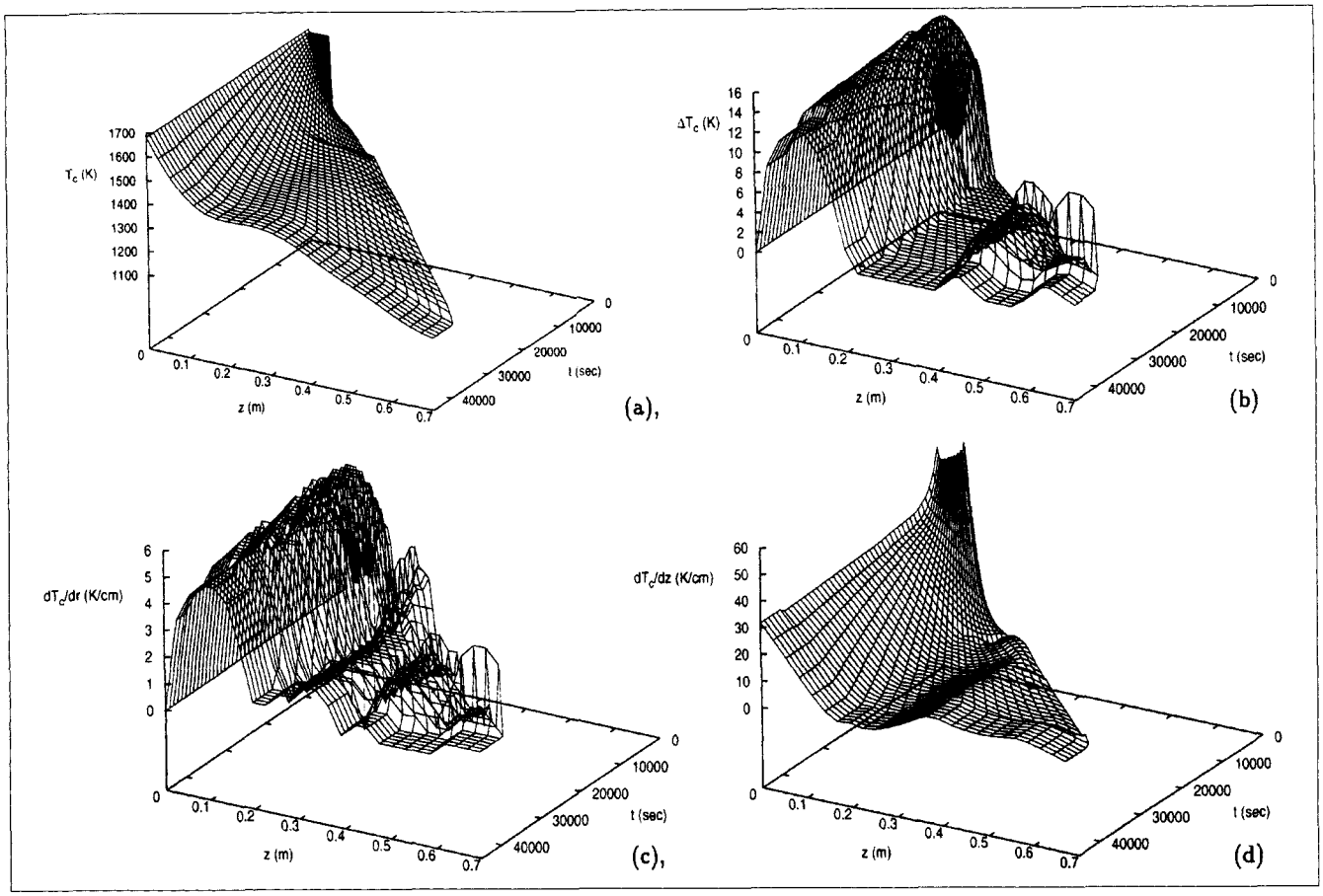

Figure 24. (a) Temperature or crystal at $r = 0.0$ m; (b) maximum temperature difference inside the crystal in the radial direction; (c) maximum thermal gradient inside the crystal in the radial direction; (d) maximum thermal gradient inside the crystal in the axial direction, as a function of time and axial coordinate under nonlinear control-exogenous disturbances.

model predictive controllers because it is of very low-order, and, therefore, it leads to optimization programs which can be rapidly solved on-line.

Remark 8: The variation of the crystal size with respect to time is a moving boundary characteristic that should be inluded in the context of controlling the thermal gradients. Of course, there are other moving boundary issues in the Czochralski process which should be included in the development of an integrated simulation of the process, however, these are not important in the context of controlling thermal gradients inside the crystal, when the crystal radius has reached a constant value.

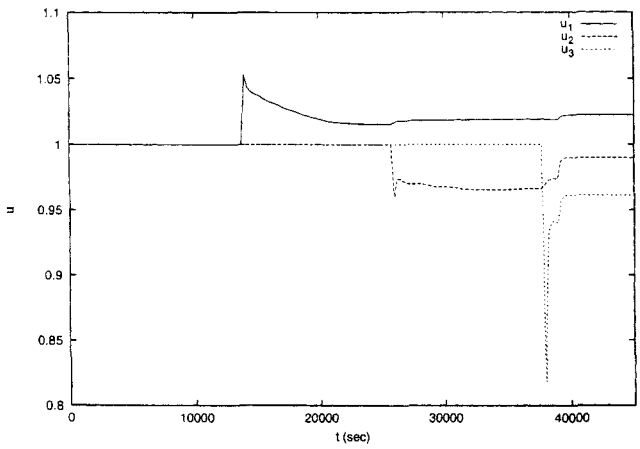

Figure 25. Manipulated input profiles-exogeneous disturbances.

Remark 9: We note that even though our study on control of the Czochralski process focused on the regulation of the temperature profile in the axial direction inside the crystal under the assumption that the crystal radius is constant, the proposed nonlinear controller can be *directly* coupled with another nonlinear controller which manipulates the pulling velocity and chamber temperature to regulate the crystal radius. This is possible because the time-scale of operation of the pulling velocity-crystal radius control loop is much faster than the time-scale of operation of the heater temperature-crystal temperature control loop, while the manipulation of the chamber temperature T_{ch} keeps the pulling velocity within specified limits, which allows decoupling the synthesis of the two controllers (see also Irizarry-Rivera and Seider (1997a) for similar conclusions). The synthesis of a nonlinear controller on the basis of an ODE model that describes the rate of change of the crystal radius as a function of the pulling velocity is presented in the appendix.

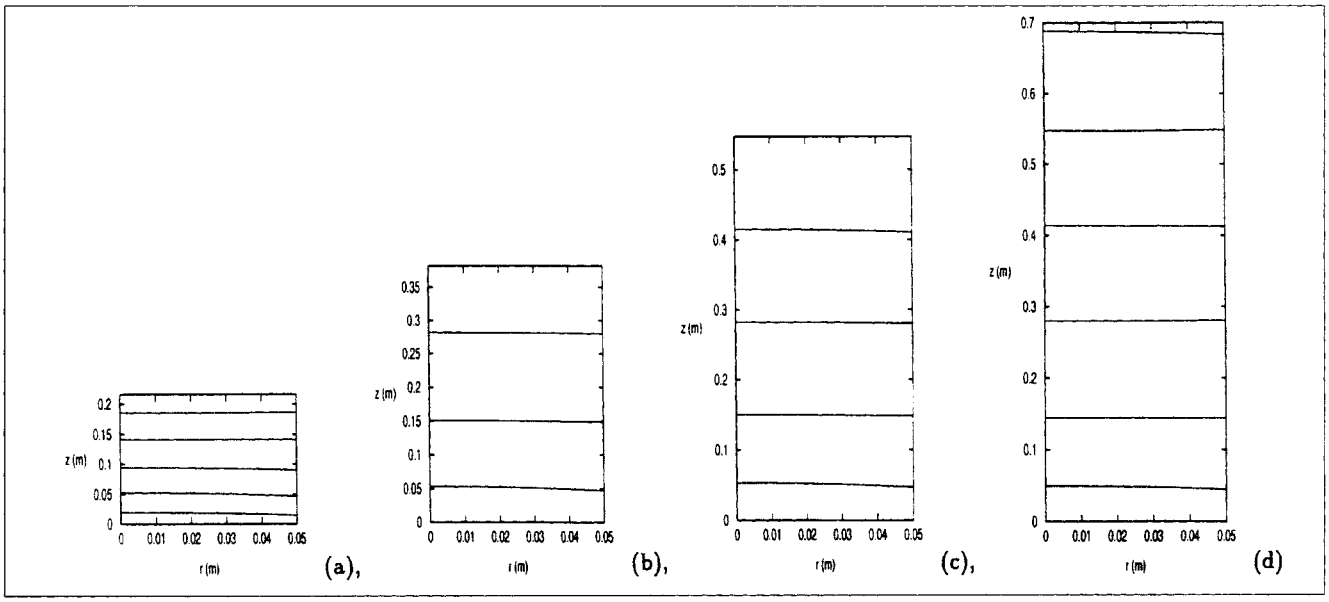

Figure 26. Temperature of crystal as a function of radial and axial coordinates under nonlinear control-unmodeled actuator and sensor dynamics.

(a) $t = 1 \times 10^4$ s; (b) $t = 2 \times 10^4$ s; (c) $t = 3 \times 10^4$ s, (d) $t = 4 \times 10^4$ s. Each contour represents a 100 K temperature difference.

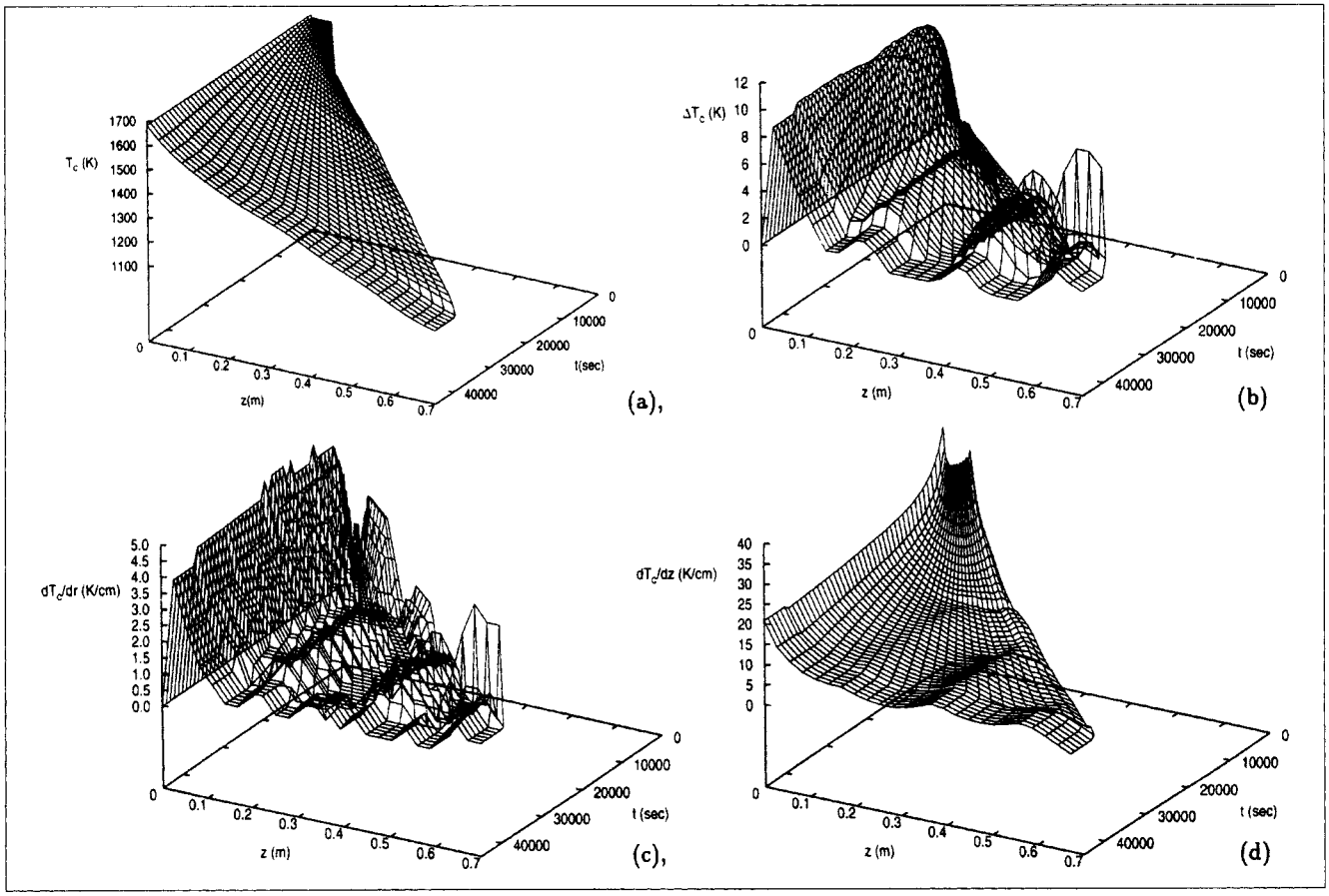

Figure 27. (a) Temperature of crystal at $r = 0.0$ m; (b) maximum temperature difference inside the crystal in the radial direction; (c) maximum thermal gradient inside the crystal in the radial direction; (d) maximum thermal gradient inside the crystal in the axial direction, as a function of time and axial coordinate under nonlinear control-unmodeled actuator and sensor dynamics.

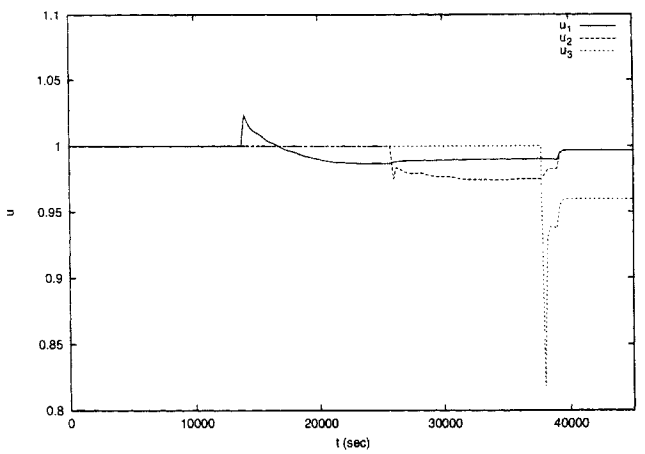

Figure 28. Manipulated input profiles-unmodeled actuator and sensor dynamics.

Conclusions

In this work, we presented a control configuration and a nonlinear multivariable model-based controller for the reduction of thermal gradients inside the crystal in the Czochralski crystal growth process after the crystal radius has reached its final value. Initially, a detailed mathematical model which describes the evolution of the temperature inside the crystal in the radial and axial directions and accounts for radiative heat exchange between the crystal and its surroundings and motion of the crystal boundary was presented. This model was used to study the behavior of the crystal temperature, formulate the control problem, design a new control configuration for the reduction of thermal gradients inside the crystal, and derive a 1-D in space PDE model with moving domain which was used for controller synthesis. The controller was synthesized by following a control method proposed in Armaou and Christofides (1999) for the synthesis of low-order (easy-to-implement) controllers for parabolic PDEs with time-dependent spatial domains. The proposed control scheme was successfully implemented on a Czochralski process used to produce a 0.7 m long silicon crystal with a radius of 0.05 m and was shown to significantly reduce the axial and radial thermal gradients inside the crystal compared to the open-loop operation and to the case of using a single control actuator. The robustness of the proposed controller with respect to parametric model uncertainty, melt, and chamber temperature disturbances and unmodeled actuator and sensor dynamics was demonstrated through simulations.

Acknowledgment

Financial support from a National Science Foundation CAREER award, CTS-9733509, is gratefully acknowledged.

Literature Cited

Armaou, A., and P. D. Christofides, "Nonlinear Feedback Contol of Parabolic PDE Systems with Time-Dependent Spatial Domains," *J. Math. Anal. Appl.*, **239**, 124 (1999).

Atherton, L. J., J. J. Derby, and R. A. Brown, "Radiative Heat Exchange in Czochralski Crystal Growth," *J. Crystal Growth*, **84**, 57 (1987).

Balas, M. J., "Feedback Control of Linear Diffusion Processes," *Int. J. Contr.*, **29**, 523 (1979).

Buchner, E. A., and T. G. J. Jones, "Capillary Phenomena part 11. Approximate Treatment of the Shape and Properties of Fluid Interface of Infinite Extent Meeting Solids and Gravitational Field," *J. C. S. Faraday*, **76**, 1419 (1980).

Chen, C. C., and H. C. Chang, "Accelerated Disturbance Damping of an Unknown Distributed System by Nonlinear Feedback," *AIChE J.*, **38**, 1461 (1992).

Christofides, P. D., *Nonlinear and Robust Control of PDE Systems: Methods and Applications to Transport-Reaction Processes*, Birkhäuser, Boston (2001).

Christofides, P. D., and P. Daoutidis, "Finite-Dimensional Control of Parabolic PDE Systems using Approximate Inertial Manifolds," *J. Math. Anal. Appl.*, **216**, 398 (1997).

Crowley, A. B., "Mathematical Modelling of Heat Flow in Czochralski Crystal Pulling," *IMA J. Appl. Math.*, **30**, 173 (1983).

Derby, J. J., L. J. Atherton, P. D. Thomas, and R. A. Brown, "Finite-Element Methods for Analysis of the Dynamics and Control of Czochralski Crystal Growth," *J. Sci. Comp.*, **2**, 297 (1987).

Derby, J. J., and R. A. Brown, "Thermal-Capillary Analysis of Czochralski and Liquid Encapsulated Czochralski Crystal Growth I. Simulation," *J. Crystal Growth*, **74**, 605 (1986a).

Derby, J. J., and R. A. Brown, "Thermal-Capillary Analysis of Czochralski and Liquid Encapsulated Czochralski Crystal Growth II. Processing Strategies," *J. Crystal Growth*, **75**, 227 (1986b).

Derby, J. J., and R. A. Brown, "On the Dynamics of Czochralski Crystal Growth," *J. Crystal Growth*, **83**, 137 (1987).

Derby, J. J., and R. A. Brown, "On the Quasi-Steady State Assumption in Modeling Czochralski Crystal Growth," *J. Crystal Growth*, **87**, 251 (1988).

Foias, C., M. S. Jolly, I. G. Kevrekidis, G. R. Sell, and E. S. Titi, "On the Computation of Inertial Manifolds," *Phys. Lett. A*, **131**, 433 (1989).

Gevelber, M. A., "Dynamics and Control of the Czochralski Process: III. Interface Dynamics and Control Requirements," *J. Crystal Growth*, **139**, 271 (1994a).

Gevelber, M. A., "Dynamics and Control of the Czochralski Process: IV. Control Structure Design for Interface Shape Control and Performance Evalution," *J. Crystal Growth*, **139**, 286 (1994b).

Gevelber, M. A., and G. Stephanopoulos, "Dynamics and Control of the Czochralski Process: I. Modelling and Dynamic Characterization," *J. Crystal Growth*, **84**, 647 (1987).

Gevelber, M. A., G. Stephanopoulos, and M. J. Wargo, "Dynamics and Control of the Czochralski Process: II. Objectives and Control Structure Design," *J. Crystal Growth*, **91**, 199 (1988).

Gevelber, M. A., M. J. Wargo, and G. Stephanopoulos, "Advanced Control Design Considerations for the Czochralski Process," *J. Crystal Growth*, **85**, 256 (1987).

Hurle, D. T. J., "Analytical Representation of the Shape of the Meniscus in Czochralski Growth," *J. Crystal Growth*, **63**, 13 (1983).

Hurle, D. T. J., *Handbook of Crystal Growth. Vol. 2: Bulk Crystal Growth. Part A: Basic Techniques*, Elsevier Science B. V., Amsterdam (1994).

Hurle, D. T. J., *Handbook of Crystal Growth Vol. 2: Bulk Crystal Growth. Part B: Growth Mechanisms and Dynamics*, Elsevier Science B. V., Amsterdam (1994).

Hurle, D. T. J., G. C. Joyce, M. Ghassempoory, A. B. Crowley, and E. J. Stern, "The Dynamics of Czochralski Growth," *J. Crystal Growth*, **100**, 11 (1990).

Irizarry-Rivera, R., and W. D. Seider, "Model-Predictive Control of the Czochralski Crystallization Process. Part I: Conduction-Dominated Melt," *J. Crystal Growth*, **178**, 593 (1997a).

Irizarry-Rivera, R., and W. D. Seider, "Model-Predictive Control of the Czochralski Crystallization Process. Part II," *J. Crystal Growth*, **178**, 612 (1997b).

Isidori, A., *Nonlinear Control Systems: An Introduction*, second edition, Springer-Verlag, Berlin-Heidelberg (1989).

Jones, D. A., and E. S. Titi, "A Remark on Quasi-Stationary Approximate Inertial Manifolds for the Navier-Stokes Equations," *SIAM J. Math. Anal.*, **25**, 894 (1994),

Leuenberger, H., and R. A. Person, "Compilation of Radiation Shape Factors for Cylindrical Assemblies," *ASME A Paper*, **56-A-144** (1956).

Ray, W. H., and J. H. Seinfeld, "Filtering in Distributed Parameter Systems with Moving Boundaries," *Automatica*, **11**, 509 (1975).
Rea, S. N., "Rapid Method for Determining Concentric Cylinder Radiation View Factors," *AIAA J.*, **13**, 1122 (1975).
Shvartsman, S. Y., and I. G. Kevrekidis, "Nonlinear Model Reduction for Control of Distributed Parameter Systems: A Computer Assisted Study," *AIChE J.*, **44**, 1579 (1998).
Siegel, R., and J. R. Howell, *Thermal Radiation Heat Transfer*, second edition, Hemisphere Publishing, Washington (1981).
Srivastava, R. K., P. A. Ramachandran, and M. P. Duduković, "Radiation View Factors in Czochralski Crystal Growth Apparatus for Short Crystals," *J. Crystal Growth*, **74**, 281 (1986).
Szabó, G., "Thermal Strain during Czochralski Growth," *J. Crystal Growth*, **73**, 131 (1985).
Temam, R., *Infinite-Dimensional Dynamical Systems in Mechanics and Physics*, Springer-Verlag, New York (1988).
Van den Bogaert, N., and F. Dupret, "Dynamic Global Simulation of the Czochralski Process: I. Principles of the Method," *J. Crystal Growth*, **171**, 65 (1997a).
Van den Bogaert, N., and F. Dupret, "Dynamic Global Simulation of the Czochralski Process: II. Analysis of the Growth of a Germanium Crystal," *J. Crystal Growth*, **171**, 77 (1997b).
Wang, P. K. C., "Control of a Distributed Parameter System with a Free Boundary," *Int. J. Contr.*, **5**, 317 (1967).
Wang, P. K. C., "Stabilization and Control of Distributed Systems with Time-Dependent Spatial Domains," *J. Optim. Theor. & Appl.*, **65**, 331 (1990).
Zhou, W., D. E. Bornside, and R. A. Brown, "Dynamic Simulation of Czochralski Crystal Growth Using an Integrated Thermal-Capillary Model," *J. Crystal Growth*, **137**, 26 (1994).

Appendix

View factors

In order to calculate the radiative heat transfer between the crystal, the surfaces of the chamber, and the surface of the melt we need to take into account the geometric relations between the corresponding surfaces. These relations are expressed by utilizing the concept of view factor. In particular, the differential view factor $dF_{1\to 2}$ is defined as the fraction of the energy which arrives at a differential black element dA_2 over the energy that leaves a differential black surface element dA_1 (Siegel and Howell, 1981). From this definition, it follows that the view factor $dF_{1\to 2}$ depends exclusively on the size of dA_2 and its orientation with respect to dA_1. The view factor definition can be extended to cover the full surfaces A_1 and A_2 and is given from the equation

$$F_{1\to 2}=\frac{1}{A_1}\int_{A_1}\int_{A_2^{vis}}\frac{\cos\beta_1\cos\beta_2}{\pi s^2}dA_2dA_1 \qquad \text{(A1)}$$

where A_1 and A_2 are the areas of the surfaces, A_2^{vis} is the area of the surface 2 which is *visible* to surface 1, β_1, and β_2 are the angles between the unit normal vectors to the corresponding surfaces and the line connecting the two points, and s is the length of this line. Based on the above definitions the following properties hold

(I) Reciprocity

$$A_2F_{1\to 2}=A_2F_{2\to 1} \qquad \text{(A2)}$$

where A_i is the surface area and $F_{i\to j}$ is the view factor of j with respect to i.

(II) The view factors of surfaces that form a complete enclosure satisfy

$$\sum_{i=1}^{n}F_{k\to i}=1, \qquad k=1,\ \ldots,\ n \qquad \text{(A3)}$$

where n is the total number of surfaces that form the enclosure.

In the process model of Eq. 1 the view factors $F_{cr\to m}(\cdot,\cdot)$, $F_{cr\to ch}(\cdot,\cdot)$, $F_{cr\to \mathrm{amb}}(\cdot,\cdot)$, $F_{cr\to i}(\cdot,\cdot)$ were separately computed by decomposing the corresponding complex geometries into simple geometries for which analytical computation of the view factors is possible. Refer to Srivastra et al. (1986) for more results on the computation of view factors for the Czochralski crystal growth process. Specifically, the following simple geometries were utilized:

Directly opposed parallel annuli (Figure A1-a) (Leuenberger and Person, 1956)

$$F_{1\to 4}=\frac{1}{2}\left[\frac{R_4^2-r_3^2}{r_1^2}-\sqrt{\left(1+\frac{R_4^2+L^2}{r_1^2}\right)^2-4\frac{R_4^2}{r_1^2}}\right.$$
$$\left.-\sqrt{\left(1+\frac{r_3^2+L^2}{r_1^2}\right)^2-4\frac{r_3^2}{r_1^2}}\right] \qquad \text{(A4)}$$

$$F_{2\to 4}=\frac{1}{2\left(R_2^2-r_1^2\right)}\left[\sqrt{\left(R_2^2+r_3^2+L^2\right)^2-\left(2r_3^2R_2^2\right)^2}\right.$$
$$-\sqrt{\left(R_2^2+R_4^2+L^2\right)^2-\left(2R_2^2R_4^2\right)^2}$$
$$+\sqrt{\left(r_1^2+R_4^2+L^2\right)^2-\left(2r_1^2R_4^2\right)^2}$$
$$\left.-\sqrt{\left(r_1^2+r_3^2+L^2\right)^2-\left(2r_1^2r_3^2\right)^2}\right] \qquad \text{(A5)}$$

Directly opposed parallel disks (Figure A1-b) (Leuenberger and Person, 1956)

$$F_{1\to 2}=\frac{1}{2}\left[1+\frac{R_2^2-L^2}{R_1^2}-\sqrt{\left(1+\frac{R_2^2+L^2}{R_1^2}\right)^2-4\frac{R_2^2}{R_1^2}}\right] \qquad \text{(A6)}$$

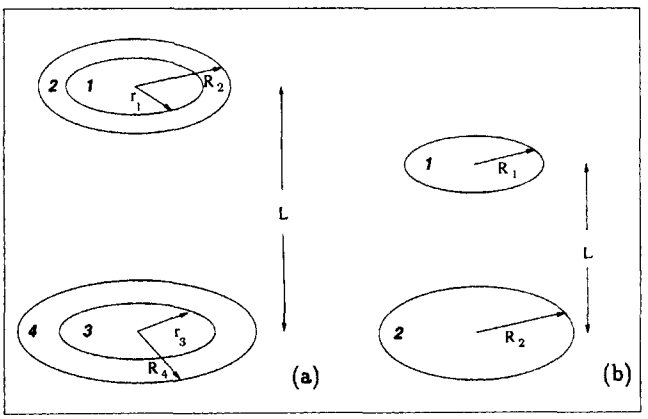

Figure A1. View factors.
(a) Annulus to annulus; (b) disk to disk.

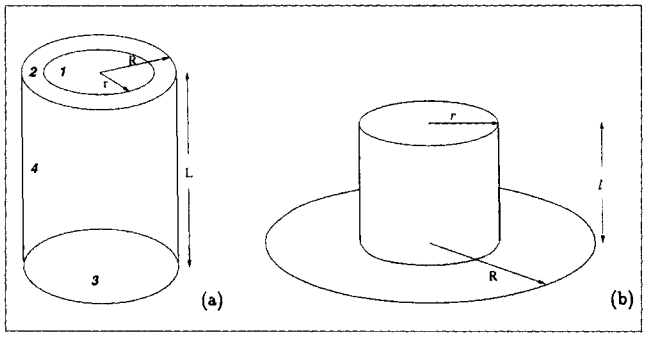

Figure A2. View factors.
(a) Annulus to cylinder, b) cylinder to disk.

Annulus to cylinder (annulus is on the top of the cylinder) (Figure A2-a) (Leuenberger and Person, 1956)

$$F_{2\to 4}=\frac{1}{2}\left[1+\frac{1}{2(R^2-r^2)}\left(L\sqrt{4R^2+L^2}-\sqrt{(r^2+R^2+L^2)^2-(2r^2R^2)^2}\right)\right] \quad \text{(A7)}$$

$$F_{1\to 4}=\frac{1}{2}\left[1-\frac{R^2+L^2}{r^2}+\sqrt{\left(1+\frac{R^2+L^2}{r^2}\right)^2-4\frac{R^2}{r^2}}\right] \quad \text{(A8)}$$

Cylinder to disk (Figure A2-b) (Rea, 1975)

$$F_{1\to 2}=\frac{1}{2\pi}\left\{\cos^{-1}\left(\frac{l^2-R^2+r^2}{l^2+R^2-r^2}\right)-\frac{r}{2l}\left[\cos^{-1}\left(\frac{r(l^2-R^2+r^2)}{R(l^2+R^2-r^2)}\right)\sqrt{\left(\frac{r^2+R^2+L^2}{r^2}\right)^2-4\frac{R^2}{r^2}}+\sin^{-1}\left(\frac{r}{R}\right)\left(\frac{l^2-R^2+r^2}{r^2}\right)-\frac{\pi(l^2+R^2-r^2)}{2r^2}\right]\right\} \quad \text{(A9)}$$

Based on the above view factors, it is possible to find the view factors between cylinders for the following two configurations:

Cylinder to cylinder (configuration I; Figure A3-a)(Rea, 1975)

$$F_{1\to 2}=1+\frac{b}{L}F_b+\frac{c}{L}F_c-\frac{L+b}{L}F_{L+b}-\frac{L+c}{L}F_{L+c} \quad \text{(A10)}$$

Cylinder to cylinder (configuration II; Figure A3-b)(Rea, 1975)

$$F_{1\to 2}=\frac{L+D}{L}F_{L+D}+\frac{Y+D}{L}F_{Y+D}-\frac{D}{L}F_D-\frac{L+Y+D}{L}F_{L+Y+D} \quad \text{(A11)}$$

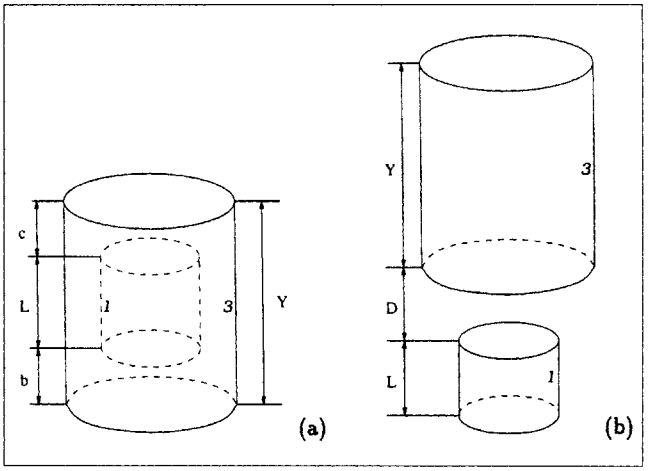

Figure A3. Cylinder to cylinder view factors.
(a) Configuration I, (b) configuration II.

where F_l denotes the view factor of Eq. A9 with the length of the cylinder being l.

Concepts of Relative Order and Characteristic Matrix

First, the Lie derivative of the scalar function $h_{0i}(t,x_s)$ with respect to the vector function $f_0(t,x_s)$ is defined as $L_{f_0}h_{0i}(t,x_s)=(\partial h_{0i}/\partial x_s)f_0(t,x_s)+\partial h_{0i}/\partial t$ for the case of time-varying h_{0i}, f_0; $L^k_{f_o}h_{0i}(t,x_s)$ denotes the k-th order Lie derivative and $L_{g0l}L^k_{f0}h_{0l}(t,x_s)$ denotes the mixed Lie derivative. Now, referring to the system of Eq. 28, we set $\mathfrak{A}_s(t)x_s+f_s(t,x_s,0)=f_0(t,x_s)$, $\mathfrak{B}_s(t)=g_0(t,x_s)$, $\mathfrak{C}_i(t)x_s=h_{0i}(t,x_s)$ to obtain

$$\frac{dx_s}{dt}=f_0(t,x_s)+g_0(t,x_s)\bar{u}_0$$
$$y_{cs_i}=h_{0i}(t,x_s) \quad \text{(A12)}$$

For the above system, the relative order of the output y_{cs_i} with respect to the vector of manipulated inputs u is defined as the smallest integer r_i for which

$$\left[L_{g0_1}L^{r_i-1}_{f0}h_{0i}(t,x_s)\cdots L_{g0_l}L^{r_i-1}_{f0}h_{0i}(t,x_s)\right]\not\equiv[0\cdots 0] \quad \text{(A13)}$$

or $r_i=\infty$ if such an integer does not exist. Furthermore, the matrix

$$C_0(t,x_s)=\begin{bmatrix} L_{g0_1}L^{r_1-1}_{f0}h_{01}(t,x_s) & \cdots & L_{g0l}L^{r_1-1}_{f0}h_{01}(t,x_s)\\ L_{g0_1}L^{r_2-1}_{f0}h_{02}(t,x_s) & \cdots & L_{g0l}L^{r_2-1}_{f0}h_{02}(t,x_s)\\ \vdots & \cdots & \vdots\\ L_{g0_1}L^{r_l-1}_{f0}h_{0l}(t,x_s) & \cdots & L_{g0_l}L^{r_l-1}_{f0}h_{0l}(t,x_s)\end{bmatrix} \quad \text{(A14)}$$

is the characteristic matrix of the system of Eq. A12.

Feedback Control of Crystal Radius

The shape of the melt-crystal interface in the Czochralski crystal growth is a complex system that varies with time and can be described by a thermal equilibrium at the interface condition, called the Stefan condition (Crowley, 1983). Analyzing this condition at the crystal-melt-air trijunction point and assuming an almost planar crystal-melt interface (Hurle et al., 1990), one can predict the difference of height between the trijunction point and the melt surface away form the melt-crystal interface, $h(t, R)$, by using the following equation (Hurle et al., 1990)

$$k_c \frac{\partial T_c}{\partial z}(R) - k_m \frac{\partial T_m}{\partial z}(R) = \Delta_m H \left(v_p - \frac{\partial h}{\partial t} \right) \quad \text{(A15)}$$

where k_c is the crystal thermal conductivity, k_m is the melt thermal conductivity, $\Delta_m H$ is the latent heat of melting, T_c and T_m are the crystal and melt temperature, respectively, and R is the crystal radius.

Approximating the heat transfer at the crystal-melt interface from the melt side in Eq. A15 with a linear temperature drop (Hurle et al., 1990), we obtain the following equation

$$k_m \frac{\partial T_m}{\partial z} \approx k_m \frac{T_m^b - T_{mp}}{h} \quad \text{(A16)}$$

where T_m^b is the temperature at the bulk of the melt. The heat transfer at the crystal-melt interface from the crystal side in Eq. A15 can be approximated by differentiating the solution of the thermal model of the process Eq. 1 (or similarly the model used for controller design) in the axial direction at position $(z, r) = (0, R)$.

The dynamics of the crystal radius are governed by the following ODE (Crowley, 1983)

$$\frac{dR}{dt} = \left(v_p - \frac{\partial h}{\partial t} \right) \tan\left(\theta_l - \theta_l^0 \right) \quad \text{(A17)}$$

where r is the radius, θ_l is the contact angle between the melt and the crystal at the trijunction point, θ_l^0 is the contact angle between the melt and the crystal at the trijunction point at steady state.

For a holm geometry of the meniscus shape, which applies to our system, the Laplace – Young equation has been solved approximately by Buchner and Jones (1980) (see Hurle (1983) for a relevant analysis) and is of the form

$$h = \left[\frac{\beta(1 - \sin\theta_l)}{1 + \frac{1}{R}\sqrt{\frac{\beta}{2}}} \right]^{1/2} \quad \text{(A18)}$$

where $\beta = \dfrac{2\sigma_s}{\rho_m g}$, σ_s is the surface tension of the melt, ρ_m is the density of the melt, and g is the acceleration of free fall.

Based on Eqs. A15–A18, we can derive the following ODE system which describes the crystal radius dynamics as a function of the heat-transfer mechanisms at the trijunction point and the pulling rate

$$\begin{aligned}
\Delta_m H \frac{d^2R}{dt^2} = & \left\{ \left[k_c \frac{\partial T_c}{\partial z}(R) - k_m \frac{T_m^b - T_{mp}}{h} \right] \right. \\
& \times \left[\tan^2\left(\theta_l - \theta_l^0 \right) + 1 \right] \frac{\partial \theta_l}{\partial R} + k_c \tan\left(\theta_l - \theta_l^0 \right) \frac{\partial^2 T_c}{\partial R \partial z}(R) \Bigg\} \frac{dR}{dt} \\
& + \left\{ \left[k_c \frac{\partial T_c}{\partial z}(R) - k_m \frac{T_m^b - T_{mp}}{h} \right] \left[\tan^2\left(\theta_l - \theta_l^0 \right) + 1 \right] \right. \\
& \times \frac{\partial \theta_l}{\partial h} + k_m \frac{T_m^b - T_{mp}}{h^2} \tan\left(\theta_l - \theta_l^0 \right) \Bigg\} \\
& \times \left\{ v_p - \frac{1}{\Delta_m H} \left[k_c \frac{\partial T_c}{\partial z}(R) - k_m \frac{T_m^b - T_{mp}}{h} \right] \right\} \quad \text{(A19)}
\end{aligned}$$

$$\frac{\partial \theta_l}{\partial h} = - \frac{2h\left(1 + \frac{1}{R}\sqrt{\frac{\beta}{2}} \right)}{\beta^2 \sqrt{1 - \left\{ 1 - \frac{h^2}{\beta^2} \left(1 + \frac{1}{R}\sqrt{\frac{\beta}{2}} \right) \right\}^2}},$$

$$\frac{\partial \theta_l}{\partial R} = \frac{h^2\sqrt{2}}{2\beta R \sqrt{1 - \left[1 - \frac{h^2}{\beta^2} \left(1 + \frac{1}{R}\sqrt{\frac{\beta}{2}} \right) \right]^2}}$$

where θ_l is given from Eq. A18 and $\partial T_c/\partial z\,(R)$, $\partial^2 T_c/\partial R \partial z\,(R)$ are given from the solution of the thermal model of Eq. 1.

Using geometric control methods (Isidori, 1989), we design a nonlinear controller which manipulates the pulling rate to stabilize the radius of the crystal at a specified value R_{set} and is of the form

$$\begin{aligned}
v_p = & \frac{1}{\Delta_m H} \left[k_c \frac{\partial T_c}{\partial z}(R) - k_m \frac{T_m^b - T_{mp}}{h} \right] \left\{ 1 + \left[\Delta_m H \frac{R_{\text{set}} - R}{\gamma_2} \right. \right. \\
& - \tan\left(\theta_l - \theta_l^0 \right) \left\{ \left[k_c \frac{\partial T_c}{\partial z}(R) - k_m \frac{T_m^b - T_{mp}}{h} \right] \right. \\
& \times \left[\tan^2\left(\theta_l - \theta_l^0 \right) + 1 \right] \frac{\partial \theta_l}{\partial R} + k_c \tan\left(\theta_l - \theta_l^0 \right) \frac{\partial^2 T_c}{\partial R \partial z}(R) \\
& \left. \left. + \Delta_m H \frac{\gamma_1}{\gamma_2} \right\} \right] \times \left[\left(k_c \frac{\partial T_c}{\partial z}(R) - k_m \frac{T_m^b - T_{mp}}{h} \right) \right. \\
& \left. \left. \times \left(\tan^2\left(\theta_l - \theta_l^0 \right) + 1 \right) \frac{\partial \theta_l}{\partial h} + k_m \frac{T_m^b - T_{mp}}{h^2} \tan\left(\theta_l - \theta_l^0 \right) \right]^{-1} \right\}
\end{aligned} \quad \text{(A20)}$$

$$\frac{\partial \theta_l}{\partial h} = -\frac{2h\left(1+\frac{1}{R}\sqrt{\frac{\beta}{2}}\right)}{\beta^2\sqrt{1-\left[1-\frac{h^2}{\beta^2}\left(1+\frac{1}{R}\sqrt{\frac{\beta}{2}}\right)\right]^2}},$$

$$\frac{\partial \theta_l}{\partial R} = \frac{h^2\sqrt{2}}{2\beta R\sqrt{1-\left[1-\frac{h^2}{\beta^2}\left(1+\frac{1}{R}\sqrt{\frac{\beta}{2}}\right)\right]^2}}$$

where the terms $\partial T_c/\partial z(R)$, $\partial^2 T_c/\partial R \partial z(R)$ are given from the solution of the reduced-order thermal model used for the design of the controller Eq. 6, θ_l is given from the solution of Eq. A18 and γ_1, γ_2 are controller parameters. The above controller ensures that the crystal radius reaches a constant value in a very small time-interval compared to the time needed to grow the entire crystal, thereby allowing to assume a constant crystal radius in the problem of regulating the thermal gradients inside the body of the crystal.

Finally, we note that the change of the melt level inside the crucible (which is much slower than the dynamics of the crystal radius) may result in a change of the position of the crystal-melt interface relative to the crucible, which in turn may lead to pulling rates which are outside prespecified limits in order to achieve a constant crystal radius. To deal with this problem, the chamber temperature T_{ch} can be used as a second manipulated variable to keep the window of operation of the pulling rate v_p within prespecified limits. The chamber temperature affects the crystal radius dynamics of Eq. A19 through the terms $\partial T_c/\partial z(R)$ and $\partial^2 T_c/\partial R \partial z(R)$ that describe the heat transfer between the crystal surface and its surroundings due to conduction and radiation at the trijunction point.

Manuscript received July 6, 1999, and revision received May 8, 2000.